Correspondence to:
J. Bumberger,
jan.bumberger@ufz.de

Broadband Dielectric Analysis of Clays: Impact of Cation Exchange Capacity, Water Content, and Porosity

Felix Schmidt[1], Norman Wagner[2], Ines Mulder[3], Katja Emmerich[4], Thierry Bore[5], and Jan Bumberger[1,6,7]

[1]Department Monitoring and Exploration Technologies, Helmholtz Centre for Environmental Research—UFZ, Leipzig, Germany, [2]Institute of Material Research and Testing—MFPA, Bauhaus-University Weimar, Weimar, Germany, [3]Department of Geography, Soil Science and Soil Resources, Ruhr-Universität Bochum, Bochum, Germany, [4]Competence Center for Material Moisture—CMM, Applied Mineralogy/Clay Science, Karlsruhe Institute of Technology—KIT, Karlsruhe, Germany, [5]School of Civil Engineering, University of Queensland, Brisbane, QLD, Australia, [6]Research Data Management—RDM, Helmholtz Centre for Environmental Research—UFZ, Leipzig, Germany, [7]German Centre for Integrative Biodiversity Research (iDiv) Halle-Jena-Leipzig, Leipzig, Germany

Abstract Clay-rich soils and sediments are key components of near-surface systems, influencing water retention, ion exchange, and structural stability. Their complex dielectric response under moist conditions arises from surface–ion electrostatics and diffuse double layers that govern transport and retention processes. This study explores the broadband dielectric spectra (1 MHz–5 GHz) of four water-saturated clays (kaolinite, illite, and two sodium-activated bentonites) in a coaxial transmission-line setup. The spectra were parameterized with two phenomenological relaxation models–the Generalized Dielectric Relaxation Model (GDR) and the Combined Permittivity-Conductivity Model (CPCM)–and two mixture models: the Augmented Broadband Complex Dielectric Mixture Model (ABC-M) and the Complex Refractive Index Model (CRIM). These approaches were evaluated for their ability to link dielectric relaxation behavior to key petrophysical parameters such as Cation Exchange Capacity (CEC), Volumetric Water Content (VWC), and porosity. The results demonstrate distinct spectral signatures correlating with clay mineralogy, particularly at low frequencies. Relaxation strength and apparent DC conductivity show systematic relationships with CEC, emphasizing the influence of clay-specific surface properties. While expandable clays like bentonites displayed enhanced relaxation due to ion-exchange dynamics, deviations in a soda-activated bentonite highlighted the impact of chemical treatments on dielectric behavior. Overall, the study highlights both the potential and the limitations of broadband dielectric spectroscopy for soil and clay characterization. This study provides a systematic framework for linking clay mineral physics to applied electromagnetic methods. The results have significant implications for non-invasive, frequency-domain methods for characterizing soils and sediments, hydrological modeling, geotechnical evaluation, and environmental monitoring.

Plain Language Summary Clay minerals are common at the Earth's surface and strongly affect how water and ions move in soils and sediments. Their dielectric behavior under moist conditions results from interactions between charged mineral surfaces and exchangeable cations. This study investigates the broadband dielectric relaxation of four clay minerals (kaolin, illite, and two sodium-activated bentonites) in the 1 MHz–5 GHz frequency range using coaxial probe measurements. We analyzed the dielectric spectra with two phenomenological relaxation models (GDR, CPCM) and two mixture models (ABC-M, CRIM) to test how well they capture links between dielectric behavior and key soil parameters such as cation exchange capacity (CEC), water content, and porosity. The results show distinct spectral signatures related to clay mineralogy. Relaxation parameters, such as relaxation strength and apparent DC conductivity, correlate with CEC and highlight the role of surface properties. Differences between the two bentonites further demonstrate how chemical treatment modifies dielectric behavior. Our findings demonstrate that broadband dielectric spectroscopy can capture key clay properties in a non-invasive way. This has potential applications for soil characterization, hydrology, geotechnics, and environmental monitoring.

1. Introduction

Soils and clay-rich geomaterials are essential components of the Earth's surface system, preserving ecological balance and ensuring human survival. They regulate the planet's water cycle, sequester carbon, and sustain food

Writing – original draft: Felix Schmidt, Norman Wagner, Ines Mulder, Katja Emmerich, Thierry Bore, Jan Bumberger

Writing – review & editing: Felix Schmidt, Norman Wagner, Ines Mulder, Katja Emmerich, Thierry Bore, Jan Bumberger

production for a growing population. However, degradation of these materials and water scarcity increasingly threaten these critical functions, emphasizing the need for advanced monitoring techniques (Cardinale et al., 2012; Gomiero, 2016; Gupta et al., 2023; Rodrigues et al., 2023; Steffen et al., 2015; United Nations General Assembly, 2015).

The productivity of clay-dominated subsurface systems relies on soil properties such as nutrient retention, water availability, and structural stability. Among these, Cation Exchange Capacity (CEC) plays a pivotal role in ion transport and surface interactions, directly influencing electrochemical behavior under changing environmental conditions. The effective CEC reflects a soil's capacity to retain and exchange positively charged ions at a given soil pH, which is essential for plant nutrition, water retention, and soil structural stability. Clay minerals, as primary constituents of soils, are—besides soil Organic Matter—critical in determining the CEC due to their high surface area and potentially high permanent layer charge. Quantifying CEC has broad implications for agricultural productivity, ecosystem health, and climate resilience strategies (Gomiero, 2016). Beyond CEC, parameters such as Volumetric Water Content (VWC) and porosity are equally vital. These properties influence hydrological modeling, soil stability, plant growth, and groundwater recharge (Guo & Lin, 2016; Vogel et al., 2024; Zacharias et al., 2024).

Traditional methods for assessing soil and sediment properties, such as chemical extractions and gravimetric measurements, are often time-consuming and unsuitable for large-scale or in-field applications, in particular for natural, clay-rich porous media where complex interactions dominate (Guo & Lin, 2016; Rodrigues et al., 2023; Weil & Brady, 2017). To overcome these limitations, broadband High Frequency Electromagnetic (HF-EM, radio to microwave) methods present a promising alternative. Although primarily applied in laboratory settings in this study, these methods are being explored for their potential in future in-field applications, including radar-based approaches for soil and agricultural monitoring (Adão et al., 2025; Huisman et al., 2003; Klotzsche et al., 2018). They leverage the relationship between dielectric permittivity and soil properties, enabling non-invasive, rapid, and scalable analyses. Previous research has shown that dielectric spectra capture the interactions between clay mineral surfaces and aqueous pore solutions, facilitating indirect estimation of parameters like CEC, VWC, and porosity (Wagner & Scheuermann, 2017; Weil & Brady, 2017).

Despite the progress in dielectric spectroscopy, significant challenges persist. The dielectric relaxation behavior of clay minerals is influenced by a multitude of complex factors, including mineralogical composition, water content, porosity, and ion exchange dynamics. Interpreting broadband dielectric spectra (spanning MHz to GHz) requires robust modeling approaches capable of isolating the contributions of overlapping relaxation processes and connecting them to critical material-specific physico-chemical parameters and connecting them to critical material-specific physico-chemical parameters (Mitchell & Soga, 2005; Santamarina et al., 2012).

In this study, we used various clays commonly found in soils as simplified soil systems to systematically investigate these relationships. The objectives of this study are as follows:

1. Experimentally determine the broadband dielectric relaxation spectra of water-saturated expansive and non-expansive clays using HF-EM methods.
2. Decompose the observed spectra into distinct relaxation processes using phenomenological and theoretical models.
3. Evaluate the potential of these models to estimate critical clay properties, including CEC, VWC, and porosity.
4. Compare the applicability of the proposed methods for advancing geomaterial characterization, with a focus on potential applications in subsurface exploration, hydrological modeling, and geotechnical analysis.

This work specifically examines kaolin, illite, and two sodium-activated bentonites to investigate the relationships between dielectric properties, CEC, VWC, porosity, and clay mineralogy. Additionally, it evaluates the performance of three modeling approaches: the Generalized Dielectric Relaxation Model (GDR), the Combined Permittivity and Conductivity Model (CPCM), and the Augmented Broadband Complex Dielectric Mixture Model (ABC-M). A comparative analysis highlights the strengths, limitations, and suitability of these models for improving geophysical and material-focused characterization methods.

In summary, this research aims to bridge the gap between fundamental clay mineral physics and applied electromagnetic techniques. By providing a foundation for non-invasive, frequency-domain dielectric analysis, it supports improved modeling of clay-rich systems in geotechnical engineering, environmental geophysics, and near-surface exploration.

2. Broadband Geoelectrical and Electromagnetic Methods and Models for Soil and Clay Characterization

Electrical and electromagnetic methods (often referred to as geoelectrical methods) have been widely applied in soil and clay sciences. A broad portion of the electromagnetic spectrum is covered, with methods operating from Direct Current (DC; Binley & Slater, 2020) up to the L-band (microwave remote sensing; Kerr et al., 2001), that is, from the mHz to the multi-GHz range–covering more than 13 orders of magnitude in frequency. Despite their differences, these methods share the same physical principles and primarily differ in their operating frequency. The main objective is to measure the electrical properties at a given frequency (or over a frequency band) and to relate these measurements to the physical and chemical properties of soils and clays. In addition to galvanic approaches, induction-based methods such as Transient or Frequency-Domain Electromagnetics (TEM/FDEM) provide non-contact alternatives that can rapidly cover large areas, especially when deployed with unmanned aircraft systems. At the HF end of the spectrum, Ground-Penetrating Radar (GPR) and microwave remote sensing represent complementary techniques, although their applicability is often limited by electromagnetic skin-depth effects in conductive soils. These field-scale approaches highlight the importance of laboratory reference data to link measurements across the full frequency spectrum and to disentangle the contributions of overlapping polarization processes.

Despite their relative success, geoelectrical methods are still confronted with significant theoretical and technical challenges. One of the main challenges is the establishment of robust quantitative relationships between measured electromagnetic parameters and underlying soils and clays properties. Addressing this challenge requires laboratory investigations of electromagnetic properties on representative soil samples under well-defined thermal, hydraulic, mechanical, and chemical boundary conditions. Such investigations are crucial because (a) they provide the necessary databases for developing the above-mentioned quantitative relationships, (b) they help identify the frequency ranges that are most sensitive to specific material properties, and (c) they offer fundamental insights into the underlying processes of electric polarization and dielectric relaxation.

The dielectric relaxation behavior of porous media contains valuable information about the material due to a strong correlation with the volume fractions of the soil phases as well as contributions by interactions between the pore solution and mineral particles (M. Han et al., 2012; Josh, 2014; Josh & Clennell, 2015; Loewer et al., 2017; Revil, 2013; Wagner et al., 2011, 2014).

There are only few systematic broadband radio to microwave (kHz to MHz) experimental investigations of saturated clays under defined mechanical conditions available for a characterization of the relaxation behavior. A decomposition of the dielectric relaxation spectra into the underlying relaxation processes is still incomplete and thus the link between the dielectric response and the petrophysical and chemical properties of soils and rocks containing clay remains insufficiently understood. An essential reason for this is the necessary combination of different measuring techniques and measuring cells (Bore et al., 2022). In addition, individual investigations on specific soils and rocks are focused on specific temperature and frequency ranges for appropriate applications (Bore, Mishra, Wagner, et al., 2021; Bore, Wagner, et al., 2021; Loewer et al., 2017). Moreover, there is a lack of protocols for experimental procedures for (a) the preparation of the soft geomaterials, that is, clay soils, and (b) installing the prepared material in measurement cells under defined hydraulic and mechanical conditions (Bore et al., 2024; Lauer et al., 2012; Schwing et al., 2016; Wagner et al., 2013).

The major parameters affecting the electrical and electromagnetic properties of soils and clays can be grouped into three categories. Following the classification of Friedman (2005), the first category describes the bulk material properties and defines the volumetric fractions of the three classical phases (solid, pore water, and air), as well as possible secondary structural configurations (e.g., aggregation), that is, porosity and VWC. The second category includes the solid particle attributes, that is, particle shape and orientation, particle size distribution, and CEC. The third category comprises the pore-water attributes, that is, ionic strength (pore-water conductivity), cation composition, and temperature. These factors do not act independently but interact in complex ways. In addition, biological activity has increasingly been recognized as a pivotal factor influencing the electrical and electromagnetic properties of soils and clays over the last two decades (Kessouri et al., 2019).

In the frequency range relevant to this study (1 MHz–5 GHz), soils and clays typically exhibit several broad and overlapping dielectric relaxation processes (Assifaoui et al., 2001; González-Teruel et al., 2020; Ishida et al., 2000, 2003; Kelleners et al., 2005; Stroud et al., 1986). Dispersion and absorption below 1 GHz are mainly controlled by

the fine-grained fraction ($<2\,\mu m$) of the material (Arcone et al., 2008), that is, by the clay content and the associated clay mineralogy. At frequencies above 1 GHz, the dielectric relaxation behavior of soils and clays is strongly correlated with the volume fractions of the soil phases and therefore contains valuable information about bulk material properties (M. Han et al., 2012; Josh, 2014; Josh & Clennell, 2015; Loewer et al., 2017; Revil, 2013; Wagner et al., 2011, 2014). A typical application is the robust estimation of soil moisture content, either via empirical calibration laws, for example, the Topp equation (Topp et al., 1980), or via material-specific calibrations.

The relaxation behavior of partially saturated and saturated soils usually shows a significant deviation from the simple Debye behavior (Debye, 1941) and a wide distribution of relaxation processes (Asano et al., 2007; Bobrov et al., 2021; Bore, Wagner, et al., 2021; Chelidze et al., 1999; González-Teruel et al., 2020; Hoekstra & Delaney, 1974; Ishida et al., 2003; Zhang et al., 2020). Therefore, the parameterization is based on corresponding dielectric relaxation models, including the Cole–Cole (Cole & Cole, 1941), Cole–Davidson (Davidson & Cole, 1951), Havriliak–Negami (Havriliak & Havriliak, 1996), Jonscher (Jonscher, 1996), KWW (Kohlrausch, 1847), and Williams–Watts (Williams & Watts, 1970) models, taking into account the expected relaxation processes in the pore solution as well as processes due to the interaction between the pore solution and the solid (Asano et al., 2007). In addition, approaches based on the Relaxation Time Distribution (RTD) provide a more physically grounded description, particularly at lower frequencies (Connolly et al., 2019).

2.1. Clay Minerals, Cation Exchange Capacity, and Electrical Double Layer

Clay minerals exhibit exceptional sorption capacity, reflected in their CEC. Typical ranges are 3–15 $cmol_c\,kg^{-1}$ for kaolinite, 10–40 for chlorite and illite, and 70–150 for smectites (e.g., montmorillonite) (Leroy & Revil, 2004). In many clays, isomorphic substitutions within the crystal structure, for example, $Al^{3+} \rightarrow Mg^{2+}$ in octahedral sheets or $Si^{4+} \rightarrow Al^{3+}$ in tetrahedral sheets, generate a permanent basal negative charge (Bourg & Sposito, 2011; Tombácz & Szekeres, 2006).

In addition to this permanent layer charge, oxide-like edge sites carry variable (pH-dependent) charge at the clay mineral–water interface. Proton uptake at these edge sites can buffer pore-water pH and influence solute adsorption, dissolution kinetics, and colloidal stability. Increasing pH and progressive deprotonation of these sites results in variable CEC. For montmorillonite, this variable CEC together with permanent layer charge yields high CEC values of roughly 70–150 $cmol_c\,kg^{-1}$ (Tournassat & Steefel, 2019). Smectites also swell due to hydration of the interlayer cations (e.g., Na^+), which further enhances their sorption capacity.

When clay minerals interact with aqueous solutions, an electrical double layer (EDL) forms to compensate surface charge not neutralized by interlayer cations. The EDL consists of a compact Stern layer, enriched in counter-ions, and a diffuse layer with excess counter-ions and a deficit of co-ions (Leroy & Revil, 2004; Revil & Leroy, 2001). Kaolinite can even develop net positive surface charge in sufficiently acidic solutions via protonation of surface oxygens (Tombácz & Szekeres, 2006). While the magnitude of the Stern potential depends primarily on surface charge density and pH, the spatial extent of the EDL is controlled by electrolyte composition and ionic strength, and the Stern-layer charge density itself varies with salinity through ion-exchange reactions in the interfacial field (Revil & Leroy, 2001).

It is important to clearly distinguish between (a) the speciation of surface charge (permanent vs. variable charge contributions) and (b) the organization of the surrounding EDL (Stern and diffuse regions). Reactive acid–base mechanisms at edge sites play a critical role in this speciation, particularly for smectites where variable edge charge densities may locally reach values comparable to permanent structural charge (Revil & Leroy, 2001). Molecular dynamics and electrostatic modeling further demonstrate that counter-ion condensation, hydration shells, and ion correlations significantly affect the EDL structure beyond the classical Gouy–Chapman–Stern picture (Bourg et al., 2007).

In swellable clay minerals such as montmorillonite, permanent interlayer charge dominates, whereas edge (variable) charge contributes comparatively little to the total CEC depending on the relative edge surface area (Delavernhe et al., 2015). In contrast, kaolinite exhibits predominantly pH-dependent edge charge, while illite combines permanent charge with a smaller variable component. Accordingly, the measured CEC is a bulk property that reflects both permanent and variable charge and depends on the measurement protocol with respect to pH. For broader reviews of electrochemical properties and complex conductivity of clays, see (Leroy et al., 2025; Maineult et al., 2025).

2.2. Overview of CEC Measurements Using Geoelectrical Methods

Among the parameters introduced above, the CEC is of paramount importance. However, measuring CEC at the field scale remains laborious, requiring extensive soil sampling and preparation steps to obtain robust, high-resolution spatial data.

Geoelectrical methods provide a promising approach for estimating CEC both in the laboratory and in the field (e. g., McLachlan et al., 2024; Mendoza Veirana et al., 2025). A short literature review of CEC measurements across the operating frequency range of these methods (mHz to GHz) is presented here. In line with the scope of this study, particular emphasis is placed on the higher frequency range using HF-EM methods.

At the lower end of the spectrum (mHz to kHz range), Induced Polarization (IP) has gained interest because of its sensitivity to polarization processes occurring at the mineral-fluid interface (Binley & Slater, 2020). Several studies have demonstrated the strong correlation between IP signals and CEC (Kettridge et al., 2008; Revil et al., 2023; Schwartz & Furman, 2014). Nevertheless, pure IP-based CEC estimation at the field scale is often ambiguous due to the interplay of CEC and moisture content on the polarization signature (McLachlan et al., 2024). Several studies (e.g., Revil et al., 2019, 2021; Soueid Ahmed et al., 2020) suggested combining resistivity and IP measurements with a petrophysical model (Dynamic Stern Layer; Revil et al., 2017) to deliver a simultaneous estimation of VWC and CEC. This approach has been successfully applied in recent field case studies combining time-domain induced polarization (TDIP) and Electrical Resistivity Tomography (ERT) with petrophysical constraints (e.g., Casotti, Revil, Ghorbani, et al., 2025; Casotti, Revil, Johnson, et al., 2025). In practice, galvanic IP/SIP surveys remain logistically more demanding than inductive HF-EM approaches because they require electrode deployment and stable ground contact (and, for SIP, multi-frequency acquisition sequences). Despite ongoing methodological and instrumental advances, dense, high-resolution mapping over large areas can still be time-consuming, leading to a practical trade-off between spatial coverage and resolution.

At intermediate frequencies (kHz to MHz range), Electromagnetic Induction (EMI) has been applied for CEC mapping. EMI can cover large areas and is quick to deploy, especially when combined with Unmanned Aircraft Systems (UAS; Vilhelmsen et al., 2024). Several studies (McLachlan et al., 2022; Triantafilis et al., 2009) reported that CEC covaried with the in-phase component of EMI measurements. This correlation was attributed to elevated iron concentrations in areas with high OM and high CEC, since the in-phase component of EMI is related to magnetic susceptibility. However, McLachlan et al. (2022) also emphasized the dependency of CEC on moisture content (through its strong relation to water retention), implying that EMI-based CEC estimates are likely to be ambiguous.

In the high-frequency range (above MHz), highly spatially resolved methods such as ground-penetrating radar (GPR; e.g., Adão et al., 2025; Huisman et al., 2003; Klotzsche et al., 2018) and microwave remote sensing (Kerr et al., 2001) are available, whereas standard frequency- and time-domain reflectometry (FDR/TDR) sensors are widely used in soil science (Robinson et al., 2003). In laboratory settings, dielectric spectroscopy techniques such as the Open-Ended probe (OE-probe; Bore, Mishra, Wagner, et al., 2021) and the Coaxial Transmission Line (CTL; Bore et al., 2016; Bumberger et al., 2018; Wagner et al., 2013) serve as reference methods and have been extensively applied in soil science (Peplinski et al., 1995; Wagner et al., 2011). The validity of these setups has been demonstrated in earlier studies using standard materials such as Polytetrafluoroethylene (PTFE) and air (Bumberger et al., 2018), as well as solvents and brines (Bore et al., 2024; Loewer et al., 2017). The validity of the measurement setup has also been verified in earlier work using reference materials such as pure water, saline solutions, and alcohols with well-known relaxation spectra (Bore et al., 2024; Loewer et al., 2017). These tests confirm the robustness of the setup across the investigated frequency range and help to identify the onset of electrode polarization effects. To date, no systematic study has focused specifically on the link between CEC and the HF-EM properties of clay-rich soils. In parallel, the borehole logging community has actively developed advanced concepts for in situ dielectric logging (e.g., Ellis & Singer, 2007; Hizem et al., 2008; Josh, 2014). To support these developments, numerous systematic studies have investigated the relationship between dielectric properties and CEC in typical reservoir rocks. For instance, Revil (2013) analyzed dielectric data from shaly sands (originally from Garrouch & Sharma, 1994) at 2 MHz and found no clear correlation between CEC and the real part of the effective complex relative permittivity, $\varepsilon_{r,eff}^{\star}$ (notations in Section 2.4). Conversely, several other studies suggest significant correlations (Benavides et al., 2023; Josh & Clennell, 2015; Stokes et al., 2020). However, it is worth noting that all of these studies relied on OE-probe techniques. Such probes are known to suffer from reduced

sensitivity below approximately 50 MHz (Wagner et al., 2013), which affects the robustness of correlations established in the lower intermediate-frequency range (1–100 MHz). In this regard, the CTL method used in the present study provides a complementary and more robust approach. Unlike OE-probes, the CTL enables broadband measurements down to 1 MHz without loss of sensitivity at the lower end of the spectrum, thus offering a reliable experimental basis to investigate potential CEC–permittivity relationships in clay-rich soils.

Josh and Clennell (2015) reported a linear correlation between $\varepsilon^{\star}_{r,eff}$ at 10 MHz and CEC for shales, using an OE-probe. Yet, such sensors suffer from reduced sensitivity below ~50 MHz, making accurate measurements in this range challenging (Wagner et al., 2013). Similarly, Benavides et al. (2023) observed a linear correlation at 1 MHz for shale samples, although the reported CEC values (0.1–0.45 $cmol_c\ kg^{-1}$) were unexpectedly low given the clay types considered, and details of the CEC determination method were not provided. Stokes et al. (2020) investigated quartz–smectite mixtures at varying matric pressures (i.e., relative humidity, RH) over 80 MHz–1.4 GHz using an OE-probe. They found strong correlations between CEC and $\varepsilon^{\star}_{r,eff}$ at 120 MHz for each RH level and proposed a semi-empirical equation to estimate CEC from known RH. This study highlights the challenge of disentangling the effects of matric pressure (or related VWC) when deriving CEC from dielectric measurements.

To support the development of new dielectric dispersion logging tools (so-called dielectric scanner; e.g., Schlumberger; Hizem et al., 2008), more sophisticated approaches based on mixture equations have been suggested (Josh & Clennell, 2015). Empirical equations have been used to correlate $\varepsilon^{\star}_{r,eff}$ at selected frequencies (10 MHz or 1 GHz) with CEC of clays and shales. The idea is to exploit dielectric dispersion in multi-frequency HF-EM measurements within multivariate approaches, as demonstrated by Garrouch (2018) for rocks originally studied by Taherian et al. (1990). Because dielectric logging tools provide only a limited number of frequency points, the number of model parameters must be kept small. For example, Pirrone et al. (2011) applied a model based on Stroud et al. (1986) with three parameters: VWC, pore-water salinity, and a so-called textural parameter, which was empirically linked to CEC. Applied to borehole logging data, this approach yielded reasonable depth profiles of estimated CEC.

This short overview highlights several key points: (a) there is a clear lack of systematic studies on the relationship between $\varepsilon^{\star}_{r,eff}$ and CEC in clays and clay-rich soils within the soil science domain; (b) from a methodological perspective, more robust approaches than the standard OE-probe are required in the high-frequency range; (c) the CTL, despite its inherent difficulties in handling samples, represents a promising alternative because it enables broadband characterization from the MHz to several GHz without the loss of sensitivity observed at the lower end of the frequency range; and (d) models developed for petroleum reservoir characterization are not directly transferable to soil physical applications. Dedicated, soil-specific modeling strategies are required to achieve quantitative, multi-parameter assessments. The present study provides an initial contribution toward this objective.

2.3. Overview of HF-EM Characterization Methods for Soil and Clay Characterization

At the laboratory scale, dielectric spectroscopy has been successfully used to investigate frequency-dependent dielectric properties over the 1 MHz–10 GHz frequency range. OE-probes have been employed in several studies since calibration and measurements are straightforward and versatile (Bore, Mishra, Bialkowski, et al., 2021; Wagner et al., 2013). Following the approach of L.-F. Chen et al. (2004), the effective complex relative permittivity $\varepsilon^{\star}_{r,eff}$ is computed from a bilinear equation and the measured scattering parameter $S_{11}(\omega)$ (reflection measurements only). This approach requires only three standards for calibration. Extensive databases are available and provide reference values at appropriate temperatures and frequencies for a broad range of liquids (Yoon et al., 2023).

Nevertheless, OE-probe measurements have well-documented limitations (Meaney et al., 2014; Wagner et al., 2013): (a) the spatial sensitivity is limited to the immediate vicinity of the probe aperture, (b) the lower frequency limit of the usable bandwidth (~50 MHz) may obscure important dielectric features of soils and clays, and (c) OE-probes should be restricted to soft materials, since accurate measurements require perfect contact between the probe and the sample surface without gaps.

In addition to the OE-probe and CTL methods employed in this study, parallel-plate capacitor setups can also be useful, even above 10 MHz, when appropriate instrumentation and calibration are available. Such capacitive approaches are often more practical in sample handling, and—when using blocking versus non-blocking electrodes

—they can help separate dielectric permittivity from conduction effects and extend reliable measurements toward lower frequencies by mitigating electrode polarization (Beloborodov et al., 2017; Josh et al., 2016). However, for clay-rich materials, electrode polarization can still impose significant limitations (Bore et al., 2025). Moreover, parallel-plate arrangements can, in principle, resolve anisotropy in natural soils and clay-rich materials, whereas coaxial waveguide geometries provide only radial fields and are therefore less suited to explicitly probing directional dielectric properties.

Waveguide methods provide a powerful alternative to the OE-probe approach. The sample is inserted into a two-port waveguide, and the full scattering matrix S_{ij} (reflection coefficients S_{11}, S_{22} and transmission coefficients S_{12}, S_{21}) is measured and used to retrieve the effective complex relative permittivity of the sample (Bumberger et al., 2018; Wagner et al., 2013). A coaxial geometry is often preferred because it does not exhibit a low-frequency cutoff (L.-F. Chen et al., 2004). A broad range of studies has employed the CTL method for investigating soils and clays. However, CTL also has drawbacks, particularly the need for advanced sample preparation techniques, which are especially critical when working with clayey materials (Bore et al., 2016, 2018).

2.4. Modeling Broadband HF-EM Material Properties

HF-EM properties of non-ferromagnetic clay soils are characterized by a complex, temperature T, pressure p, and frequency f dependent, effective relative permittivity $\varepsilon_{\mathrm{r,eff}}^{\star}(T,p,\omega)$, electrical modulus $M_{\mathrm{eff}}^{\star}(T,p,\omega) = \varepsilon_{\mathrm{r,eff}}^{\star}(T,p,\omega)^{-1}$, or effective electrical conductivity $\sigma_{\mathrm{eff}}^{\star} = j\omega\varepsilon_0\varepsilon_{\mathrm{r,eff}}^{\star}$, with angular frequency $\omega = 2\pi f$ (Loewer et al., 2017). These quantities are complex and can be expressed in terms of their real and imaginary parts.

$$\varepsilon_{\mathrm{r,eff}}^{\star}(\omega) = \varepsilon_{\mathrm{r,eff}}'(\omega) - j\varepsilon_{\mathrm{r,eff}}''(\omega)$$
$$M_{\mathrm{eff}}^{\star}(\omega) = M_{\mathrm{eff}}'(\omega) + jM_{\mathrm{eff}}''(\omega) \tag{1}$$
$$\sigma_{\mathrm{eff}}^{\star}(\omega) = \sigma_{\mathrm{eff}}'(\omega) + j\sigma_{\mathrm{eff}}''(\omega)$$

Here, these properties are essential for understanding the dielectric response of soils under varying environmental and mechanical conditions. Typical spectra are presented in Figure 1.

In general, soils and rocks containing clay minerals exhibit several distributed relaxation processes. These processes are key to interpreting dielectric spectra and understanding the complex interaction between soil phases and electromagnetic waves.

2.4.1. Phenomenological Relaxation Models

In order to model broadband dielectric spectra of soils and rocks, a generalized dielectric relaxation model (GDR) based on Cole-Cole terms can be applied (Loewer et al., 2017; Wagner et al., 2011, 2013).

$$\varepsilon_{\mathrm{r,cc}}^{\star} - \varepsilon_{\infty} = \sum_{i=1}^{k} \frac{\Delta\varepsilon_i}{1 + (j\omega\tau_i)^{b_i}} - j\frac{\sigma_{\mathrm{DC}}'}{\omega\varepsilon_0} \tag{2}$$

Here, ε_0 is the dielectric permittivity of vacuum, ε_{∞} is the relative constant permittivity at the high frequency limit, $\Delta\varepsilon_i$ is the relaxation strength, τ_i is the relaxation time, $0 \leq b_i \leq 1$ is the stretching exponent of the i-th relaxation process, and σ_{DC}' is the apparent direct current conductivity.

There is strong evidence that HF-EM properties above 1 GHz are dominated by water relaxation processes (Loewer et al., 2017; Robinson et al., 2003; Wagner et al., 2011, 2013, 2014), which can be modeled using a single Debye term ($b_{1,\mathrm{water}} = 1$, α-process). Dispersion and absorption at frequencies below approximately 1 GHz are typically modeled with two additional Cole-Cole terms (α', β) to account for interfacial relaxation processes (Wagner et al., 2011, 2013). This approach results in $k = 3$ for Equation 2.

When using the effective relative permittivity $\varepsilon_{\mathrm{r,eff}}^{\star}(\omega)$ to characterize relaxation processes, it becomes evident that DC-conductivity dominates the relaxation behavior in the range of $f \leq 1$ MHz. For low-frequency (LF, $f \leq 1$ MHz) modeling, it is often advantageous to use the effective electrical conductivity $\sigma_{\mathrm{eff}}^{\star}$ instead. This
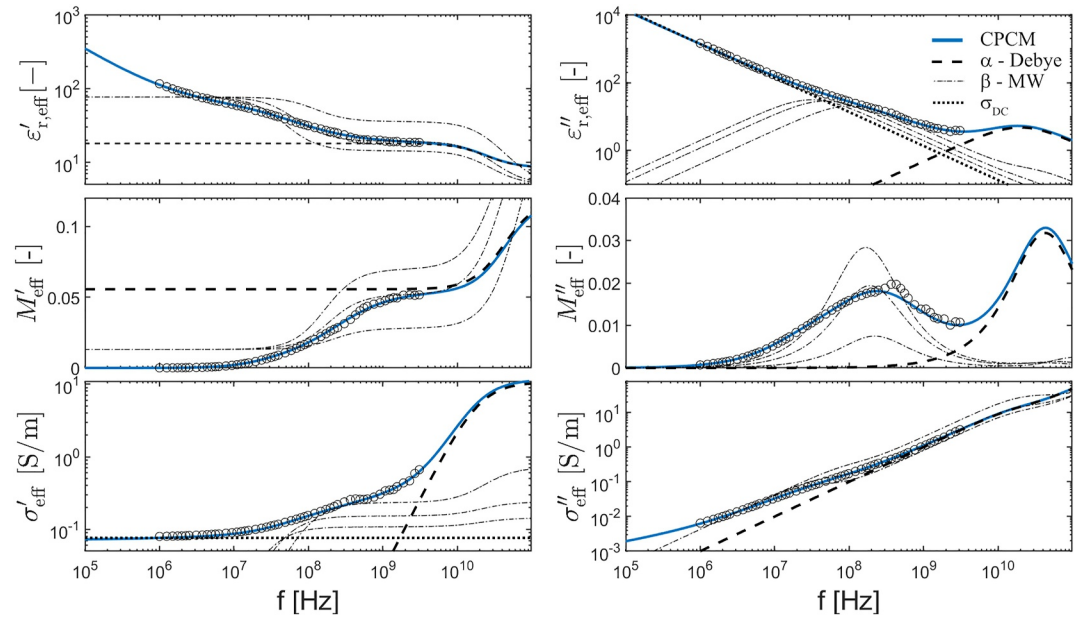
Figure 1. From top to bottom: Real and imaginary part of the complex effective permittivity $\varepsilon_{r,eff}^{\star}$ of a nearly water saturated loess soil (cf. Loewer et al., 2017), volumetric water content $\theta = 0.36$ m³/m³, porosity $\phi = 0.37$, water saturation $S_W = 0.98$), complex electrical modulus $M^{\star}$ and complex effective conductivity $\sigma_{eff}^{\star}$ as a function of frequency. The solid line represents a theoretical prediction of the measured spectra using the Complex Permittivity and Conductivity Model according to Loewer et al. (2017). The dashed line is computed with a Debye-type relaxation function (process P1), the dash-dotted line is a single Maxwell-Wagner effect (cf. Bore, Wagner, et al., 2021) calculated based on the approach by Bona et al. (1998), and the dotted line indicates the direct current conductivity contribution to the spectra.

approach avoids the high values of relaxation strength associated with permittivity-based models in the LF range. Moreover, polarization parameters such as the chargeability of specific processes can be related to soil properties like CEC using the Dynamic Stern Layer model (Revil et al., 2017). However, permittivity-based models are more suitable for analyzing HF relaxation processes and can be effectively linked to theoretical mixture models (Wagner et al., 2011, 2013).

To combine these advantages, the Combined Permittivity and Conductivity Model (CPCM) was proposed by Loewer et al. (2017). This model integrates both permittivity- and conductivity-based approaches to cover the entire frequency spectrum. It includes a Debye term for water relaxation at high frequencies, a permittivity-based Cole-Cole term for intermediate frequencies, and a conductivity-based Cole-Cole term for low frequencies. It is worth noting that dielectric-based analysis becomes particularly informative above ~1 MHz, since in lossy materials the phase and amplitude of transmitted signals are relatively insensitive to permittivity at lower frequencies, whereas the joint phase–amplitude response provides richer and more diagnostic information at higher frequencies.

$$\varepsilon_{r,eff}^{*} = \varepsilon_{\infty} + \frac{\Delta\varepsilon_1}{1 + (j\omega\tau_1)^{c_1}} + \frac{\Delta\varepsilon_2}{1 + (j\omega\tau_2)^{c_2}}$$
$$-j\frac{\sigma_{dc}'}{\omega\varepsilon_0}\left[1 + \frac{M'}{1 - M'}\left(1 - \frac{1}{1 + (j\omega\tau_3)^{c_3}}\right)\right]$$

(3)

Here, $0 \leq c_i \leq 1$ are stretching exponents, and M' represents the apparent chargeability. According to the definition by Seigel (1959) chargeability is linked to DC-conductivity σ_{dc}' and instantaneous conductivity σ_{∞} of the appropriate relaxation process through the relationship $\sigma_{dc}' = \sigma_{\infty}(1 - M')$ (see Loewer et al., 2017 for details).
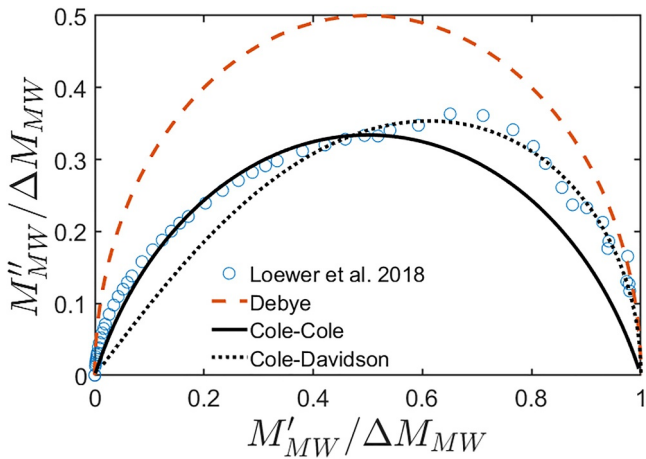
Figure 2. Representation of the complex modulus for Maxwell-Wagner polarization normalized with the modulus strength between 1 MHz and 1 GHz, $\Delta M_{\mathrm{MW}} = \varepsilon'^{-1}_{\mathrm{r,\,eff}}(f = 1\ \mathrm{GHz})$, in the Gaussian plane.

In this study, apparent HF-chargeability M' is estimated using the relaxation mode as described by Weigand and Kemna (2016). This hybrid modeling framework allows for the characterization of both HF and LF processes, enabling more accurate interpretation of dielectric spectra across wide frequency ranges.

Figure 2 illustrates the Maxwell-Wagner polarization in the complex modulus representation. A pure Maxwell-Wagner process leads to a Debye-type relaxation, while distributed processes produce more generalized behaviors. These can be modeled using the Havriliak-Negami-type modulus representation (Havriliak & Havriliak, 1996).

$$\frac{M_i^{\star}}{\Delta M_i} = \frac{(j\omega\tau_i)^{\alpha_i \cdot \beta_i}}{(1 + (j\omega\tau_i)^{\alpha_i})^{\beta_i}} \tag{4}$$

Here, ΔM_i represents the modulus strength of the i-th process, τ_i the relaxation time, and $0 \le \alpha_i, \beta_i \le 1$ the stretching exponents. For $\alpha_i = \beta_i = 1$, Equation 4 reduces to a Debye function. For $\alpha_i = 1$, it simplifies to a Cole-Davidson function, and for $\beta_i = 1$, it becomes a Cole-Cole function.

In addition to such phenomenological formulations, physics-based approaches such as the Differential Effective Medium (DEM) theory have been proposed to describe broadband dielectric properties of porous media (e.g., Cosenza et al., 2003; Y. Chen & Or, 2006; González-Teruel et al., 2020). While DEM-based models can reproduce spectra in a forward modeling framework, their application for inverse modeling of frequency-domain dielectric data remains limited. To the authors' knowledge, no successful examples exist in which DEM has been used to invert dielectric spectra of clay-rich soils. In our own tests with related models such as the Bussian approach on granular media, parameters obtained from inversion often lacked physical meaning (e.g., cementation exponents close to unity). In contrast, the extended volume-averaging approach underlying the ABC-M model provides a more robust framework for linking dielectric dispersion with petrophysical parameters in an inverse modeling context.

2.4.2. Broadband Dielectric Mixture Models

Theoretical mixture models provide a robust framework for describing the effective dielectric properties of soils, considering their multiphase composition. A widely used approach is the Complex Refractive Index Model (CRIM), which relates the effective permittivity to the individual contributions of soil phases (Arcone et al., 2008; Schön, 2015; Wang & Schmugge, 1980).

$$\varepsilon_{\mathrm{r,mix}}^{\star\ 0.5} = \theta\varepsilon_{\mathrm{r,W}}^{\star\ 0.5} + (1 - \phi)\varepsilon_{\mathrm{G}}^{0.5} + (\phi - \theta) \tag{5}$$

Here, θ represents the VWC, ϕ the porosity, and ε_{G} the permittivity of the solid particles.

The electromagnetic properties of the solid particles are, strictly speaking, a second-order tensor (dyadic) with nine independent material parameters (Schön, 2015). However, for practical applications, the relative effective permittivity of the solid matrix material ε_{G} can be estimated based on the mineralogical composition of the solid phases, assuming quasi-isotropy at the sample scale (Robinson, 2004a, 2004b; Robinson & Friedman, 2003). A lack of systematic broadband frequency- and temperature-dependent high-resolution electromagnetic investigations under defined stress-strain conditions on mono- and poly-crystalline mineral phases remains a significant limitation (Boivin et al., 2022a, 2022b; Jones & Friedman, 2000). Addressing this issue is crucial for advancing the accuracy of theoretical mixture models.

To estimate ε_{G}, several empirical relationships have been proposed that link the relative effective permittivity of a material to its grain density ρ_G (in g/cm^3). Notable examples include

$$\varepsilon_{\mathrm{G}} = A^{\rho_G} \tag{6}$$

as suggested by Olhoeft (1981), with $A = 1.93 \pm 0.17$, or by Campbell (2002), with $A = 1.96$. Another widely used empirical equation was introduced by Dobson et al. (1985).

$$\varepsilon_G = \left(1.01 + 0.44 \, \rho_G\right)^2 - 0.062 \tag{7}$$

In this study, ε_G was determined as the geometrical mean of Equations 6 and 7. To compute the complex permittivity of the aqueous pore solution $\varepsilon^\star_{r,W}$, a modified Debye model was employed.

$$\varepsilon^\star_{r,W} - \varepsilon_\infty = \frac{\varepsilon_{s,W} - \varepsilon_\infty}{1 + j\omega\tau_W} - j\frac{\sigma_W}{\omega\varepsilon_0} \tag{8}$$

Here, ε_∞ represents the high-frequency limit, $\varepsilon_{s,W}$ the quasi-static relative permittivity, and τ_W the relaxation time. Debye parameters were calculated using equations from Kaatze (2007) and Buchner et al. (1999). The DC conductivity of the pore water, σ_W, was treated as an unknown parameter determined via inverse modeling (see Section 3.4).

In addition to the CRIM model, the Augmented Broadband Complex Dielectric Mixture Model (ABC-M) was applied, as proposed by Bore et al. (2018). The model was originally developed by Pride (1994) using a volume-averaging approach to derive an expression for the high-frequency dielectric constant (i.e., the real part of the effective relative permittivity) of a two-phase medium. It was later extended to partially saturated conditions by Linde et al. (2006) and generalized by Revil (2013) to account for both effective complex conductivity and relative permittivity. The ABC-M combines this Volume-Averaging (VA) formulation with an additional phenomenological relaxation term to represent dielectric dispersion:

$$\varepsilon^\star_{r,eff}(\omega) = \frac{\Delta\varepsilon_{cc}}{1 + (j\omega\tau_{cc})^{b_{cc}}} + \varepsilon^\star_{r,\,VA} \tag{9}$$

where the VA effective permittivity is given by:

$$\varepsilon^\star_{r,\,VA} = \phi^m \left[S_W^n \varepsilon^\star_{r,W} + \left(1 - S_W^n\right) + (\phi^{-m} - 1)\varepsilon_G\right] \tag{10}$$

Here, $S_W = \theta/\phi$ denotes water saturation, while n and m are the saturation and cementation exponents, respectively. This combination of relaxation and volume-averaging makes ABC-M a versatile tool for analyzing soil dielectric properties under diverse conditions, particularly for clay-rich soils where complex interactions dominate. In practice, n and m can be approximated as $n \approx m = m_0 + \text{CEC}m_1$, with $m_0 = 1.8$ and $m_1 = 4.3 \cdot 10^{-5}$ kg/C. This simplifies Equation 10 as follows:

$$\sigma'_{eff} \approx \theta^m \sigma'_w + \theta^{m-1} \sigma'_s \tag{11}$$

$$\varepsilon^\star_{r,eff} \approx \theta^m \varepsilon^\star_w + (1 - \theta^m)\varepsilon_G \tag{12}$$

where σ'_{eff} represents the effective conductivity, σ'_w the real electrical conductivity of the pore fluid, $\sigma'_s = \sigma_{s,1.3\ GHz} = (0.44 \pm 0.1)$ S/m, according Revil (2013), the real surface conductivity contribution, and $\varepsilon^\star_w$ the complex permittivity of the pore solution.

2.4.3. Empirical and Semi-Empirical Approaches

Early studies extensively explored the empirical relationship between soil water content and high-frequency (≈ 1 GHz) relative permittivity. A foundational empirical equation relating VWC θ to apparent relative permittivity ε_A was proposed by Topp et al. (1980) based on Time Domain Reflectometry (TDR) measurements with CTL:

$$\varepsilon_A = 3.03 + 9.3 \, \theta + 146.0 \, \theta^2 - 76.7 \, \theta^3 \tag{13}$$

This equation has been widely used for characterizing soil water content due to its simplicity and effectiveness in many soil types.

Wensink (1993) systematically investigated the frequency dependence of relative effective permittivity $\varepsilon_{r,eff,W} = \varepsilon'_{r,eff}$ and effective electrical conductivity $\sigma_{eff,W} = j\omega\varepsilon_0\varepsilon''_{r,eff}$ over a range from 1 MHz to 3 GHz. Empirical equations for specific frequencies, including 5 MHz, 50 MHz, and 1 GHz, were derived. For this study, the equation for 1 GHz is particularly relevant:

$$\varepsilon_{r,eff,WS}(f = 1\ GHz) = 3.2 + 41.4\ \theta + 16.0\ \theta^2 \tag{14}$$

This empirical approach effectively correlates VWC with relative permittivity at high frequencies.

Josh and Clennell (2015) introduced a method to determine the dispersion of the real part of the permittivity by calculating the difference between its values at 1 GHz and 1 MHz:

$$\Delta\varepsilon_{1GHz} = \varepsilon'_{r,eff}(f = 1\ MHz) - \varepsilon'_{r,eff}(f = 1\ GHz) \tag{15}$$

This approach enables the characterization of superimposed relaxation processes with relaxation frequencies below the bulk water relaxation frequency. However, it does not establish a direct relationship between soil physical properties and specific relaxation mechanisms. Instead, it identifies correlations between dispersion behavior and clay mineralogy.

In addition to dispersion analysis, DC conductivity contributions can be determined from the spectral plateau of the measured real part of the complex conductivity (refer to Figure 1). The depression of the imaginary part in the modulus representation within the complex plane provides further insight into distributed relaxation processes, such as Maxwell-Wagner polarization, physical bound water features, and counter-ion effects.

3. Materials and Methods

To cover a CEC range of 4.4–110 cmol$_c$ kg^{-1}, four different clay samples were selected, each containing typical primary clay minerals (see Table 1). The mineral proportions were determined by X-ray diffraction (XRD), confirming the dominant clay minerals in each sample. XRD was conducted using a Bruker D8 Advance A25 diffractometer, equipped with a LynxEye XE detector (Bruker AXS GmbH, Karlsruhe, Germany). Cu-Kα radiation was used to record the diffraction patterns, and Rietveld refinement was carried out using the open-source program Profex (Döbelin & Kleeberg, 2015). While the XRD analysis identifies Na-smectite and dioctahedral mica as distinct phases (Table 1), the presence of illite–smectite mixed-layer structures cannot be excluded, and some of the mica fraction may in fact represent interstratified phases.

The two bentonite samples were activated with sodium carbonate, converting calcium bentonite into sodium bentonite. This process is commonly used in industrial applications to prevent rapid sedimentation of clay materials in water suspensions. According to the manufacturer, bentonite 1 received more sodium carbonate than bentonite 2, resulting in overactivation with respect to the CEC, that is, sodium carbonate was added in excess of the cation exchange capacity of the bentonite. Under such conditions, part of the carbonate remains in the pore water without being adsorbed on exchange sites (Kaufhold et al., 2013). Consequently, bentonite 1 contains an oversupply of ions in solution that are not adsorbed on the clay mineral surfaces.

3.1. Material Preparation

The dry samples of illite and bentonites were mixed with deionized water until saturation, exceeding the liquid limit of the clay. This ensured that air-filled macro-pores were avoided. The sample holder, a 60 mm-long CTL, was sealed at the lower end with a PTFE ring, as shown in Figure 3. Detailed construction and dimensions of the sample holder are described in (Lauer et al., 2012).

The sample holder was placed on top of the suspension and allowed to sink freely into the material due to gravity (Figure 4, left). The samples were then left to dry and shrink at room temperature for several days. To prevent the formation of cracks and voids, the suspension container was placed on a vibration table and shaken every 2 hr for 15 min.

Table 1
X-Ray Diffraction (XRD) Data of the Four Investigated Clays

Clay	%	Minerals
Kaolin	82	Kaolinite
	9	Dioctahedral mica
	9	Quartz; traces of accompanying minerals
Illite	68	Dioctahedral illite 1M
	11	Kaolinite
	6	Trioctahedral mica
	5	Dioctahedral mica
	10	Calcite; feldspar (microcline); quartz; hematite
Bentonite 1	67	Na-saturated dioctahedral smectite (montmorillonite)
	13	Dioctahedral mica
	7	Quartz
	6	Calcite
	5	Dolomite
	2	Trioctahedral mica; feldspar (microcline)
Bentonite 2	92	Na-saturated dioctahedral smectite (montmorillonite)
	8	Aragonite; calcite; feldspar (plagioclase); quartz

Note. Note that "bentonite 1" and "bentonite 2" in column one refer to industrial bentonite samples, that is, clayey materials dominated by smectite. The actual clay mineral identified by XRD is smectite (montmorillonite), listed in column three.

When the material began forming cracks that did not close upon shaking, the sample holder was removed, cleaned, and the surface of the material was leveled (Figure 4, right). This preparation resulted in nearly fully saturated clay/water mixtures, which remained stable when the holder was inverted. Strictly speaking, complete saturation in fine-textured clay samples can only be achieved under vacuum conditions with degassed solutions. In our study, we attempted to approach full saturation by allowing the samples to equilibrate with the aqueous solution until pressure equilibrium was reached.

Samples of illite 1 and illite 2 were derived from the same raw material. However, illite 1 was dried for a longer duration, resulting in lower water content and reduced porosity. Vertical inhomogeneities in water content can occur when the sample is stored with the PTFE ring pointing downward. To mitigate this, the filled sample holder was sealed airtight and stored with the PTFE ring facing upwards. The sealing was later removed, and the sample was inserted into the Vector Network Analyzer (VNA) adapter unit (Figure 5). The right adapter was mounted on a sliding rail, allowing parallel movement relative to the left adapter. This setup prevented lateral forces on the sample and ensured proper alignment of the inner and outer conductors.

The influence of the PTFE rings was subsequently removed using high-frequency (HF) de-embedding techniques and the dielectric properties of PTFE (Bumberger et al., 2018; Keysight-Technologies, 2017). In the frequency range used, PTFE is approximated as $\varepsilon'_r = 2.1$ and $\varepsilon''_r = 0.003$. The homogeneity of the samples was verified by comparing the scattering parameter reflection factors from the left (S_{11}) and right (S_{22}) sides, which should match for homogeneous samples.

The kaolin samples were prepared differently. The clay powder was dried in an oven at 60°C and then sprayed with demineralized water until a gravimetric water content of $w = 0.2$ was achieved. This mixture was compacted in a 4-inch mold according to ASTM-D698-7e1 (ASTM, 2009) method, ensuring reproducible porosity and density of the water-saturated sample. The material was then cut from the mold with a hydraulic press and placed in the sample holder, as described in Bore et al. (2016).

Unlike other samples, the use of a PTFE ring was unnecessary for kaolin. To achieve full saturation, the cut-out sample with the coaxial cell was placed on a ceramic plate in demineralized water for 24 hr. During this period, the sample absorbed water, resulting in slight swelling and increased porosity. Excess material that leaked from the cell was removed before inserting the sample into the VNA fixture.

3.2. Physical and Chemical Parameters

Physical parameters collected in Tables 2 and 3 were determined using standard methods. Gravimetric water content was calculated by weighing small sample portions before and after oven drying. Samples were dried at 105°C for 24 hr and re-weighed. Sample ID602 was dried at 60°C until its mass stabilized, which likely resulted in slightly lower gravimetric water content than the actual value.

Porosity was calculated based on gravimetric measurements, the measurement cell volume, and the particle density provided by the clay supplier. Volumetric water content was derived using the density of water at 21°C. Water saturation was calculated as the ratio of water volume to pore volume. With the described preparation, saturation was close to 1, with an estimated error of ±0.04.
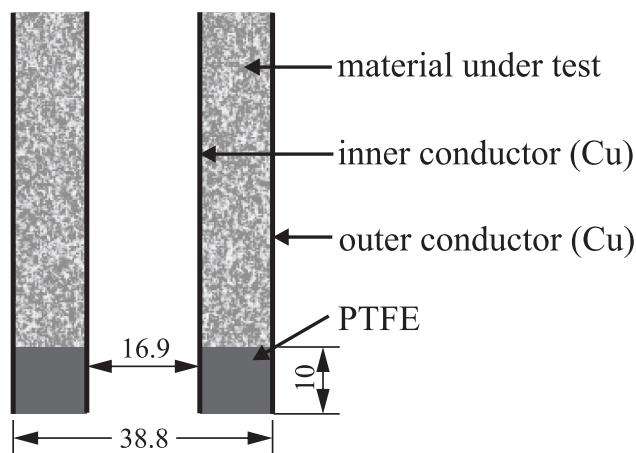

Figure 3. Cross-section of the complete coaxial cell sample holder, featuring Polytetrafluoroethylene rings at the lower end. The upper end is left unsealed. Dimensions are given in millimeters.

Figure 4. Left: Empty coaxial cell with a Polytetrafluoroethylene ring inserted into a clay-water suspension. Right: Prepared bentonite sample in the coaxial cell, prior to insertion into the measurement adapter.

Key material properties were further characterized to facilitate comparison with other studies. CEC was measured by the Cu-trien method according to Meier and Kahr (1999) with changes according to Steudel et al. (2009).

The ratio of CEC to Specific Surface Area (SSA) is directly related to the surface charge density of clay minerals. This concept has been discussed in the context of membrane efficiency and electrochemical surface interactions (e.g., Chang et al., 2018; Leroy & Revil, 2004; Revil, 2013). The SSA was determined using nitrogen adsorption based on the Brunauer-Emmett-Teller (BET) theory. For non-swellable clay minerals a correlation of SSA with CEC was observed. In swellable clays, such as bentonites, the SSA primarily indicates platelet size of the smectite (Delavernhe et al., 2015). In swellable clays, such as bentonites, BET-derived SSA values primarily reflect the external platelet size of smectite (Delavernhe et al., 2015). It should be noted, however, that when using the
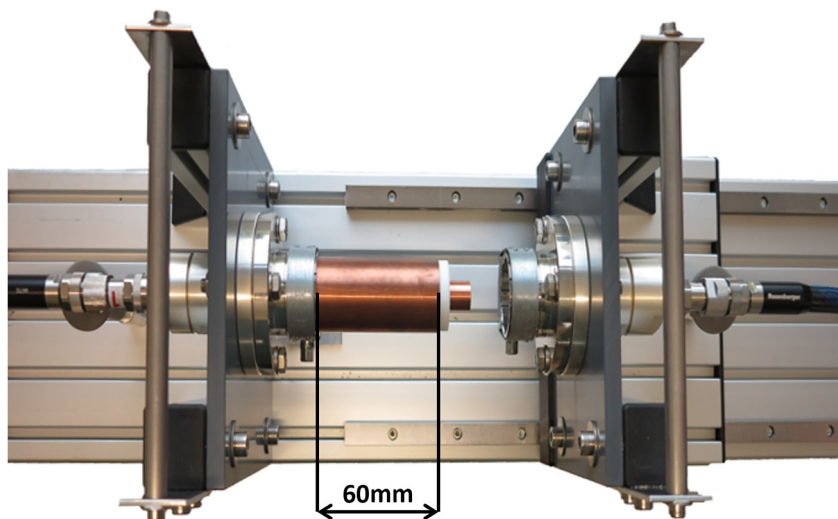

Figure 5. CTL cell with adapter units and coaxial cables leading to the Vector Network Analyzer ports. The material under test, here a white PTFE part, is placed as a dielectric between the copper-made inner conductor and the outer conductor of the cell.

Table 2
Physical Parameters of the 15 Investigated Clay Samples

Clay name	σ_w $\frac{S}{m}$	$\sigma_{DC,fit}$ $\frac{S}{m}$	ϕ -	θ $\frac{m^3}{m^3}$	w $\frac{kg}{kg}$	ID
Kaolin	0.37	$7.5 \cdot 10^{-2}$	0.49	0.46	0.34	ID602
	0.25	$6.27 \cdot 10^{-2}$	0.53	0.56	0.46	ID644
	0.24	$6.29 \cdot 10^{-2}$	0.54	0.55	0.46	ID645
Illite 1	0.49	0.12	0.52	0.52	0.41	ID626
Illite 2	0.19	0.10	0.75	0.73	1.09	ID630
	0.19	0.10	0.75	0.72	1.09	ID631
Bentonite 1	0.76	0.67	0.94	0.95	6.18	ID808
	0.67	0.61	0.96	0.97	9.00	ID822
	0.68	0.62	0.97	0.99	10.33	ID823
	0.70	0.65	0.96	0.97	9.00	ID824
	0.68	0.65	0.97	0.99	11.33	ID825
Bentonite 2	0.36	0.31	0.96	0.96	8.38	ID809
	0.29	0.25	0.97	0.97	12.65	ID834
	0.32	0.27	0.97	0.96	11.99	ID840
	0.42	0.34	0.95	0.94	8.33	ID844

Note. The water saturation is determined to be $S = 1(\pm0.04)$. σ_w: direct current conductivity of the pore water, inverted with the Complex Refractive Index Model (CRIM); $\sigma_{DC,fit}$: direct current conductivity fitted to low-frequency data (Equation 16); ϕ: porosity; θ: volumetric water content; w: gravimetric water content; ID: sample identifier.

Ethylene Glycol Monoethyl Ether (EGME) method to determine the Total Specific Surface Area (TSSA), a strong correlation between SSA and CEC is observed for both swelling and non-swelling clays. Particle density, measured with a helium pycnometer, reflected the density of the solid components. Particle density, measured with a helium pycnometer, reflected the density of the solid components. The permittivity of the solid particles, ϵ_G, was estimated from empirical relations with grain density (Equations 6 and 7). It should be noted, however, that direct evidence for these estimates is limited, and solid mineral permittivities are generally considered to be around ~5.5 for uncharged phases.

It should be noted that in this study we did not determine the formation factor F using the classical conductivity approach with aqueous solutions of varying salinities. Instead, all experiments were performed close to the iso-conductivity point. This choice was motivated by (a) the time-consuming nature of the systematic salinity series required for clay-rich samples and (b) the lack of reference measurements on standard materials (e.g., glass beads) in the high-frequency range with our setup at the time of this study. The approach chosen here ensures internal consistency and comparability within our data set. Future work, building on recent developments by Bore et al. (2025), will address the determination of formation factors at higher salinities in a systematic manner.

To compare DC pore water conductivities among the clays, demineralized water was added well above saturation. Clay-to-water mixing ratios of 1:5 and 1:20 were prepared to observe the effect of soda activation. Centrifugation was used to extract pore water, and its conductivity was measured. Higher CEC correlated with higher pore water conductivity. However, bentonite 1 exhibited excess ions beyond surface adsorption capacity, causing its pore water conductivity to remain higher than bentonite 2 even at increased water content.

3.3. Experimental Setup

In this investigation, the CTL, as shown in Figure 5, served directly as the sample holder (Bumberger et al., 2018; Lauer et al., 2012; Schmidt et al., 2021; Wagner et al., 2013). Using adapter units and coaxial cables, the transmission line was connected to the VNA (.e^{5}071C, Keysight Technologies Inc., Santa Rosa, CA, US). The

Table 3
Physical Parameters and Mean Values per Clay Type

Clay name	CEC $\frac{cmol_c}{kg}$	BET $\frac{m^2}{g}$	ρ_G $\frac{g}{cm^3}$	ϵ_G —	$\sigma_{DC}(1:5)$ $\frac{S}{m}$	$\sigma_{DC}(1:20)$ $\frac{S}{m}$	$\bar{\sigma}_{DC,fit}$ $\frac{S}{m}$	$\bar{\sigma}_w$ $\frac{S}{m}$	$\bar{\phi}$ —	$\bar{\theta}$ $\frac{m^3}{m^3}$	$\bar{w}$ $\frac{kg}{kg}$
kaolin	4.4	16	2.63	5.46	$7.89 \cdot 10^{-3}$	$5.35 \cdot 10^{-3}$	$6.69 \cdot 10^{-2}$	0.29	0.52	0.52	0.42
illite 1	18	105	2.67	5.59	$1.92 \cdot 10^{-2}$	$1.25 \cdot 10^{-2}$	0.12	0.49	0.52	0.52	0.41
illite 2							0.1	0.19	0.75	0.73	1.09
bentonite 1	74	51	2.68	5.62	0.32	0.24	0.64	0.70	0.96	0.97	9.17
bentonite 2	110	70	2.65	5.59	0.41	0.15	0.29	0.35	0.97	0.96	10.34

Note. The water saturation is determined to be $S = 1(\pm0.04)$. BET: specific surface area determined with the Brunauer–Emmett–Teller (BET) method; note that for clay minerals, in particular swelling clays, BET tends to underestimate the total active surface area compared to methods such as the Ethylene Glycol Monoethyl Ether (EGME) method; ρ_G: particle density measured with a helium pycnometer; ϵ_G: permittivity of the solid particles (Equations 6 and 7); σ_{DC}: direct current conductivity of extracted porewater from two clay-water ratios; $\sigma_{DC,fit}$: fitted direct current conductivity of the measured samples (Equation 16); σ_w: direct current conductivity of the pore water, inverted with the Complex Refractive Index Model (CRIM); ϕ: porosity; θ: volumetric water content; w: gravimetric water content.

VNA measured the scattering parameters (S_{ij}) from 300 kHz up to 5 GHz, characterizing the reflection and transmission behavior of the material under test. For the present study, the analysis was restricted to frequencies $f \geq 1$ MHz to avoid low-frequency artifacts and to focus on the HF-EM range.

To ensure accuracy, the influences of the cables and the analyzer were eliminated through a standard calibration with an electronic calibration kit (ECal N4431B, Keysight Technologies Inc., Santa Rosa, CA, US). The N-male to 1 5/8″ adapter units (SPINNER GmbH, Munich, Germany) introduced an error in the form of a phase shift. This phase shift was determined using a short-standard in place of the measurement cell and subsequently removed by HF de-embedding (Bumberger et al., 2018; Keysight-Technologies, 2017). The dielectric permittivity spectra were calculated from the *S*-parameters using the Backer Jarvis Iterative (BJI) algorithm as described in Lauer et al. (2012), Wagner et al. (2013), and Schwing et al. (2016).

3.4. Inverse Parameter Estimation

To go beyond simple real and imaginary part models, the proposed models were used to investigate the underlying relaxation mechanisms in the materials. The full set of four scattering parameters was parameterized using a Shuffled Complex Evolution Metropolis algorithm (SCEM-UA; Vrugt et al., 2003). This global optimization algorithm combines the strengths of the Metropolis algorithm, controlled random search, competitive evolution, and complex shuffling. It efficiently estimates the optimal parameter set and its underlying posterior distribution within a single optimization run (Heimovaara et al., 2004).

For the CRIM model, most parameters were determined directly through measurement or assumed based on established properties. However, the pore water conductivity σ_w was estimated using a differential evolution algorithm (Storn & Price, 1997). This approach allowed for a robust and systematic estimation of material parameters, enabling deeper insights into the dielectric properties and relaxation processes of the clay materials. The inverted σ_w values showed reasonable agreement with the directly measured pore-water conductivities (Table 3), typically within the same order of magnitude. Noticeable deviations were observed for bentonite 1, where over-activation led to an excess of ions in solution, resulting in higher measured values compared to the inversion-based estimates.

3.5. Model Vector and Parameter Boundaries

In order to define the inversion problem explicitly, the model vector was parameterized by the relaxation parameters of the three approaches (GDR, CPCM, ABC-M). We used a uniform distribution within specified parameter boundaries as a quasi non-informative prior, instead of Jeffreys' prior (Tarantola, 2005). The parameter boundaries were chosen according to physical reasoning and experimental constraints, and they span a broad range to ensure robustness (see Table 4). This strategy follows previous work on electromagnetic inversion of porous media proposed by Wagner et al. (2011), later refined by Bumberger et al. (2018) and Bore et al. (2024).

Table 4 summarizes the structure of the model vector. The chosen parametrization allows the estimated model parameters to be directly linked to physico-chemical properties such as water saturation, porosity, and CEC. However, it should be noted that the parameterization of low-frequency processes ($f < 10$ MHz; β/cc) is subject to high uncertainty due to limited bandwidth. This can lead to equivalence problems in synthetic inversions, where different parameter combinations reproduce similar spectral features. Broadband measurements, as suggested by Bore et al. (2022, 2025), are therefore essential to obtain robust parameter estimates.

4. Results

4.1. General Observations of Permittivity Spectra

The measured permittivity spectra for all clay samples are presented in Figure 6. The frequency dependence of the real part of the permittivity for the two expansive clays is nearly identical, indicating similar dispersion. However, the imaginary part shows marked differences below 2 GHz, reflecting a stronger DC-contribution for bentonite 1 without affecting relaxation strength.

In the lower frequency range below 10 MHz, the real parts exhibit permittivity values that far exceed those of the individual phases (water, clay, air), indicating strong dispersion across all clay samples. This trend flattens at higher frequencies, approaching the GHz-limit of the effective relative permittivity. Meanwhile, in the lower

Table 4
Model Vector and Parameter Boundaries for the Three Inversion Approaches

Parameter	GDR-min	GDR-max	CPCM-min	CPCM-max	ABCM-min	ABCM-max
α/1-process	–	–	–	–	–	–
ε_∞	1	10	1	10	–	–
$\Delta\varepsilon$	0	100	0	100	–	–
τ [s]	$1.e^{-14}$	$1.e^{-10}$	$1.e^{-14}$	$1.e^{-10}$	$1.e^{-14}$	$1.e^{-10}$
ε_G	–	–	–	–	1	10
S_w	–	–	–	–	0.9	1
ϕ	–	–	–	–	0.2	1
m	–	–	–	–	1	10
n	–	–	–	–	1	10
α'/2-process	–	–	–	–	–	–
$\Delta\varepsilon$	0	$1.e^5$	0	$1.e^5$	–	–
τ [s]	$1.e^{-12}$	$1.e^{-7}$	$1.e^{-12}$	$1.e^{-7}$	–	–
b	0	1	0	1	–	–
β/3/cc-process	–	–	–	–	–	
$\Delta\varepsilon$	0	$1.e^{10}$	–	–	0	$1.e^{10}$
m'	–	–	0	1	–	–
τ [s]	$1.e^{-7}$	1	$1.e^{-7}$	1	$1.e^{-12}$	1
b/c	0	1	0	1	0	1
σ_{DC}/σ'_W [S/m]	0	10	0	10	0	10

Note. Uniform priors were used within the listed ranges. GDR, Generalized Dielectric Relaxation model; CPCM, Cole–Cole type polarization–conduction model; ABC-M, Augmented Broadband Complex model.

frequency range ($f \leq 100$ MHz), the typical $1/f$-dependency of the conductivity contribution is evident in the imaginary parts. Around 1 GHz, dielectric losses due to pore water relaxation dominate, causing an increase in the imaginary part (i.e., losses).

Modulus representation (Figure 6) reveals significant polarization processes between 10 MHz and 1 GHz, which are obscured in the permittivity plots by low-frequency effects. The peaks of the imaginary part curves align approximately with the critical frequency ($\varepsilon''/\varepsilon' = 1$), which determines the transition between dielectric polarization effects and conductivity effects.

The results highlight a strong dependence of dielectric properties on the CEC, water content, and porosity. For example, bentonite 1, with its elevated CEC and porosity due to overactivation, shows unique dielectric dispersion and relaxation strength compared to kaolin and illite. These findings demonstrate the critical role of CEC and porosity in modulating the electromagnetic properties of clay materials (Figure 6).

Figure 7 compares the measured data to the pure Maxwell-Wagner process modeled by a Debye-function (see Equation 4 and Figure 2). The values were normalized to the real part of the modulus at the frequency of the local minimum (around 1 GHz) of the imaginary part; $\Delta M_{MW} = M'_{MW}(f_{loc.min.})$. This frequency was determined by smoothing the curve, calculating the first derivative, and identifying its zero crossings. The similarity between the measured curves and the ideal model is evident. However, deviations arise due to superimposed processes, such as physical bound water features and counter-ion effects.

The pronounced DC conductivity σ_{DC} of water-saturated clays causes a masking of other relaxation processes in the imaginary part of the effective relative permittivity, extending far into the MHz range. To reveal these masked processes, the influence of DC conductivity must be removed. Using the RF measurement data, the apparent DC conductivity σ'_{DC} can be determined as follows. Assuming that $\sigma'_{eff} = -\omega\varepsilon_0\varepsilon''_{r.eff}$ and that σ'_{eff} is dominated by σ'_{DC} in the frequency range from 300 kHz to 1 MHz, the following function is fitted to the measured data of $\varepsilon''_{r.eff}$:
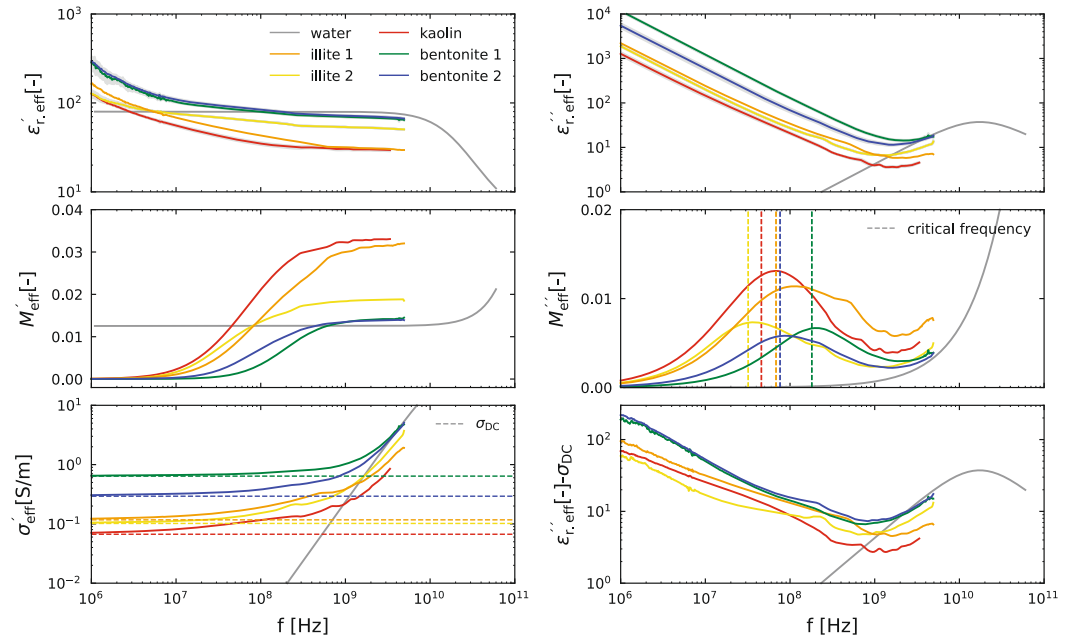
Figure 6. Permittivity spectra of all four clays, together with the spectra of water according to Equation 8 with values from Kaatze (2007) at 21°C and $\sigma_w = 0$. For this plot, the mean values and standard deviation of the permittivity at each frequency point were determined for each clay type (kaolin, illite, bentonite 1, and bentonite 2). The standard deviation is shown as a gray area. At the critical frequency ($\varepsilon''/\varepsilon' = 1$), the dielectric behavior shifts from conductor to dielectric. The modulus $M^\star$ and effective electrical conductivity $\sigma^\star_{\text{eff}}$ are defined as in Figure 1. In the lower right plot, the influence of the DC conductivity on the imaginary part has been removed to make other relaxation processes visible.

$$\varepsilon''_{\text{r.eff}} = \varepsilon_{\infty,\text{app}} - \frac{\sigma'_{\text{DC}}}{\varepsilon_0 \omega} \tag{16}$$

Figure 7. The complex electrical modulus $\left(M^\star_{\text{eff}} = \varepsilon^{\star -1}_{\text{r,eff}}\right)$ calculated from the mean permittivity for each clay material in a Cole-Cole plot. The value of $\Delta M_{\text{MW}} = M'_{\text{MW}}(f_{\text{loc.min.}})$ used for normalization is based on the frequency of the local minimum of M_{eff} around 1 GHz. The MW-Debye curve describes the relaxation behavior of a pure Maxwell-Wagner process, modeled by a Debye function (see Equation 4 and Figure 2).

The fitting parameters are the apparent RF limit of permittivity $\varepsilon_{\infty,\text{app}}$ and σ'_{DC}. In Figure 8, the measured and fitted data are plotted together to illustrate the suitability of Equation 16 and its underlying assumptions. The results of this fit are further applied in Figure 6 and summarized in Table 3.

The values of porosity and water content vary significantly depending on the dominant clay mineral (see Table 2). Expansive clays such as bentonite 1 and 2 exhibit higher porosity under saturation conditions compared to non-expansive clays like kaoline and illite. This variation in porosity under water-saturated conditions is reflected in the HF range due to its correlation with the VWC θ. Nonetheless, the analysis enables conclusions regarding the impact of mineralogical and physicochemical properties—including particle size distribution, SSA, clay mineralogy, and cation exchange capacity—on the dielectric relaxation behavior below 1 GHz (cf. Figure 6).

The dependence of the permittivity at 1 GHz on the VWC is well-established (Topp et al., 1980). Figure 9 illustrates this relationship for the measured samples at 1 GHz. For comparison, the empirical Topp formula (Equation 13) and the model by Wensink (Equation 14) are also plotted. The results show that the real part of the permittivity increases with VWC, eventually approaching the pure water values (e.g., Kaatze, 2007) at saturation for high porosity. This behavior aligns with expectations based on the quadratic
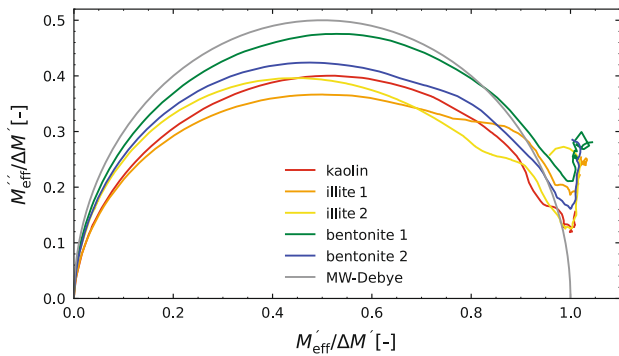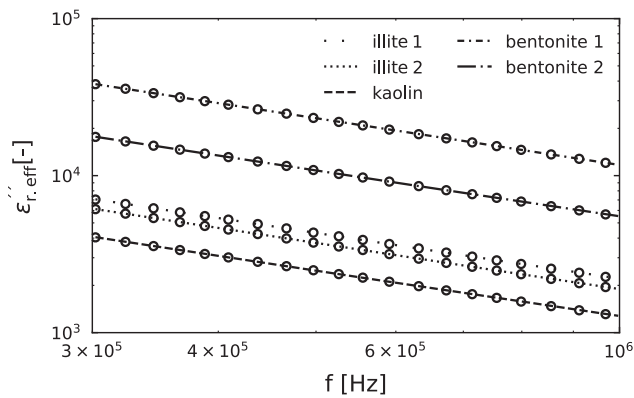
Figure 8. Measurement data (circles) and σ_{DC}-fit (lines) of the imaginary part of the effective relative permittivity from 300 kHz to 1 MHz for the four clay materials.

polynomial nature of Equation 13. However, for higher water contents or porosities, the Wensink model introduces larger errors in describing the measured results.

Since the data presented here aligns with well-known correlations, the validity of the measurements can be confidently assumed. A typical observation is that the real part of the permittivity values remains below those predicted by the Topp formula. This phenomenon is characteristic of clayey soils (Wagner & Scheuermann, 2009) and remains a subject of ongoing research. Investigations by González-Teruel et al. (2020) highlight the significant role of porosity and geometrical factors, such as particle shape, orientation, and size distribution, compared to confined or bound water.

The imaginary part of the dielectric permittivity characterizes the energy losses associated with electromagnetic wave propagation in the material. These losses comprise both dielectric losses and conduction losses. In the lower frequency range, conduction losses dominate and are primarily determined by the direct current conductivity.

Figure 9 also demonstrates that the conductivity of water-saturated samples and bentonite suspensions varies with clay type and water content. Notably, variations in water content within a clay type have a minor influence on conductivity. Furthermore, the conductivities of water-saturated clays correlate positively with the CEC and clay type, as reported by Bore et al. (2022). Although comparing conductivities across different clay-water ratios introduces potential errors, the trend remains evident. This trend is further supported by examining conductivity values at fixed mixing ratios in Table 3.

A similar trend is observed in the imaginary part $\varepsilon''_{r,eff}$(1 GHz), where grouping by clay type and sorting by ascending CEC is evident. While the frequency here is an order of magnitude higher, this behavior suggests that the influence of DC conductivity on the imaginary part extends into the lower GHz range. As polarization losses in water become more prominent, they contribute increasingly to the total losses, reducing the relative influence of clay material-specific losses.

4.2. Direct Dispersion Analysis

An approach to analyze the dielectric spectra of clay-containing soils and rocks is to evaluate the spectra at specific frequencies, as described in Josh and Clennell (2015). Figure 10 presents the values for $\varepsilon^*_{r,eff}$ plotted against the CEC at $f = 1$ MHz and $f = 10$ MHz for both the real and imaginary components.

At 1 and 10 MHz, the effective relative permittivity demonstrates clear correlations with CEC and water content. Notably, the imaginary part shows a strong positive correlation with CEC, distinguishing clay types effectively (Figure 10). The results also emphasize that higher water content and porosity, as seen in bentonite samples, amplify relaxation processes, particularly at lower frequencies, where conductivity dominates.

The real part of the effective relative permittivity $\varepsilon'_{r,eff}$ shows a positive correlations with CEC beside the impact of water saturation and porosity. Notably, $\varepsilon'_{r,eff}$ at 10 MHz seems a robust indicator distinguishing clay types effectively (Figure 10). However, $\varepsilon''_{r,eff}$ at low frequencies or appropriate real part of effective conductivity is statistically more robust, as evidenced by the height of the boxplots, and provides valuable insights due to its variation with CEC (Revil, 2013). In Figure 10, the different clay materials are distinctly identifiable by the imaginary part of the effective permittivity. Furthermore, the clays with low CEC exhibit relatively small values of the $\varepsilon''_{r,eff}$, consistent with expectations. Notably, the imaginary parts at CEC = 74 cmol$_c$ kg^{-1} are higher compared to those at CEC = 110 cmol$_c$ kg^{-1}.

Josh and Clennell (2015) discussed that electrode polarization is relevant even in permittivity spectra below 10 MHz obtained by capacitance methods. However, this frequency range also includes effects such as Maxwell-Wagner polarization, ionic conduction in the porous network, and restricted ion mobility within the EDL (Revil, 2013). The Maxwell-Wagner effect results in permittivities that far exceed those of individual components and depends strongly on material contrast, surface area, and the volume fractions of minerals and fluids (Josh & Clennell, 2015).
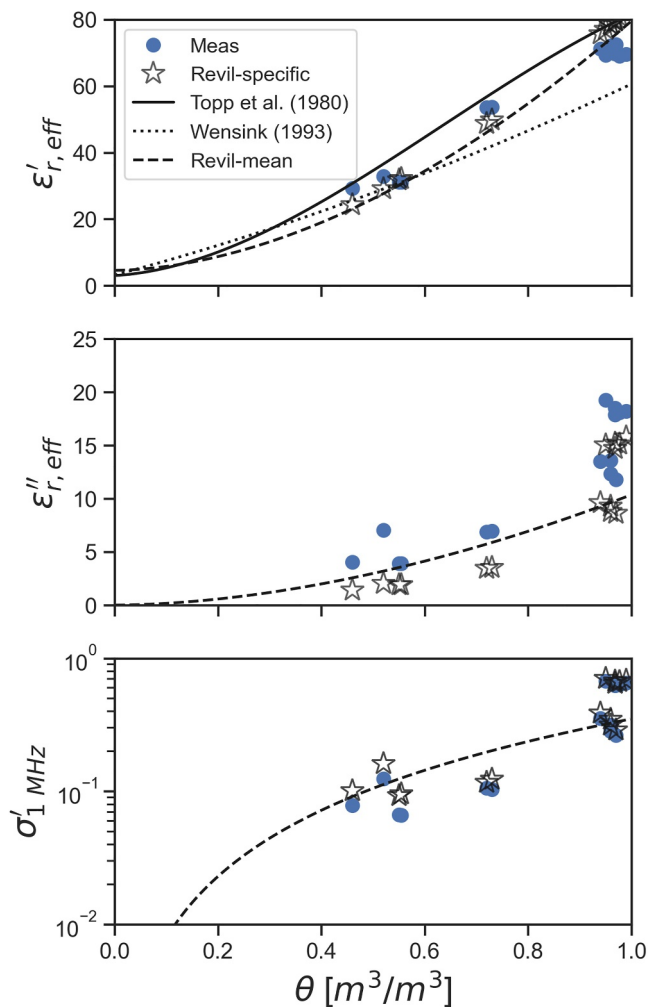
Figure 9. The relative effective permittivity of all samples at $f = 1$ GHz as a function of volumetric water content. Additionally, the DC conductivity extrapolated from 1 MHz ($\sigma_{1\,MHz} = \varepsilon''_{r,eff}(1\,MHz)2\pi f \varepsilon_0$) is shown in the third plot. The legend applies to all plots. The Topp equation (Topp et al., 1980), the model from Revil (2013, see Equations 11 and 12), and the Wensink equation (Wensink, 1993, see Equation 14) are plotted as references. The Revil-specific values correspond to individual samples, while the Revil mean refers to the mean values across all samples for the material parameters in Equations 11 and 12.

In the frequency range above 10 MHz, pore geometry effects on dielectric losses become less pronounced. Consequently, spectral analyses at $f > 10$ MHz are less sensitive to interference. In this range, charge transport paths are shortened, and as a result, the Maxwell-Wagner effect dominates, while double-layer effects have a minor impact on the dielectric relaxation behavior. This shift enhances the influence of clay surface charge effects on the dielectric spectrum. Materials with a larger surface area or higher CEC exhibit greater polarizability, leading to higher real parts of the effective permittivity.

This trend is evident when comparing the two frequency points in Figure 10. The real parts of the permittivities at $f = 10$ MHz show a clear positive correlation with CEC and exhibit reduced data spread. In opposition to Josh and Clennell (2015) we did not find a linear trend but a more complex trend. In contrast, at $f = 1$ MHz, the data spread within each clay type is more substantial, likely due to additional effects influencing polarizability at lower frequencies. An additional observation emerges from comparing the imaginary parts at the two frequency points. The imaginary part values at $f = 1$ MHz and $f = 10$ MHz differ by approximately a factor of 0.1, supporting the assumption of $1/f$-dependence for the imaginary component and the dominance of apparent DC conductivity.

4.3. Decomposition of the Dielectric Spectra

The results of the inverse parametrization of the measured S-parameters using the described models are shown in Figures 11, 13, 15, and 16. Except for the CRIM, the models accurately describe the dielectric responses of the clays. The parametrizations effectively reproduce the spectral curves, as depicted in the figures. To highlight the differences in the modeling approaches, the individual relaxation contributions are also included in the diagrams.

For the GDR model, the relaxation contributions include RF-water relaxation depicted as α, intermediate relaxation as α', and low-frequency relaxation as β. In the kaolin example (Figure 11), these components are distinctly identifiable. Comparing results for the different clays (Figure 12) reveals that for illite, kaolin, and bentonite 2, the relaxation strength of the α' process remains relatively consistent, with values ranging from 8.9 to 25.2. In contrast, bentonite 1 exhibits significantly higher relaxation strength, varying from 44.7 to 129.7, reflecting the overactivation with sodium carbonate in this sample.

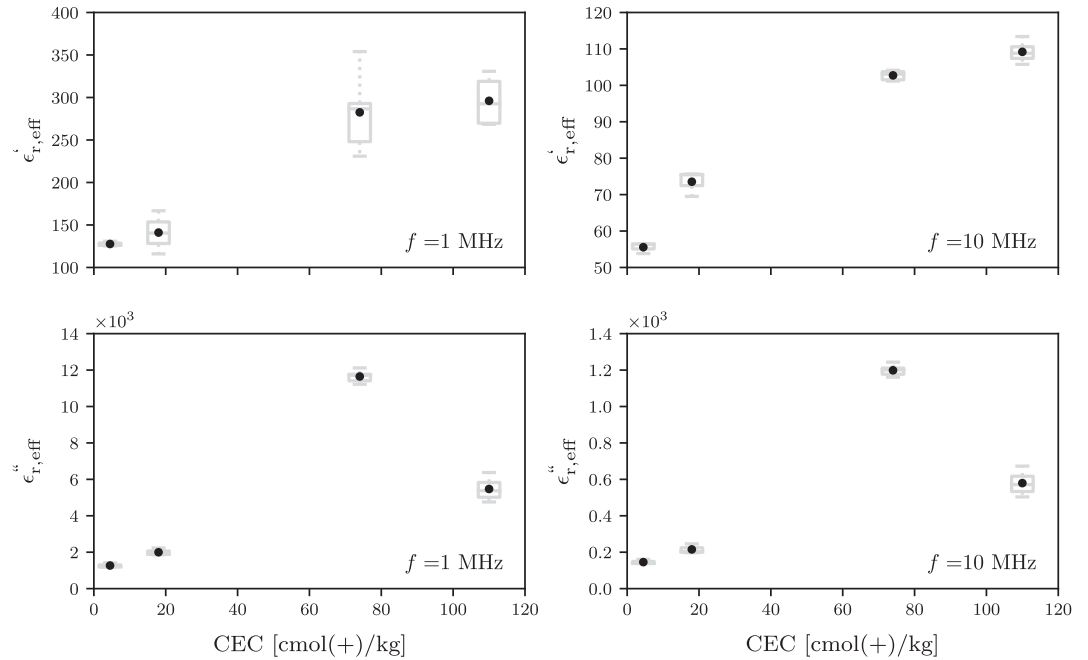The CPCM is particularly noteworthy because it incorporates low-frequency conductivity parameters, such as the apparent chargeability M', to model the lower frequency range (see Equation 3). As described by Revil et al. (2017), the normalized chargeability $M_n = M\sigma_\infty = \sigma_\infty - \sigma_0$ provides insight into the correlation between relaxation parameters and soil properties. However, since σ_∞ is not directly available as a parameter in the model, M_n is calculated as $\sigma'_{dc}M'/(1 - M')$.

The GDR model confirms the dependence of relaxation strength on CEC, water content, and porosity (Figure 13). For instance, the α' relaxation strength of bentonite 1 is significantly higher (44.7–129.7) than that of kaolin and illite (8.9–25.2), correlating with its high CEC and porosity. This demonstrates the influence of CEC on low-frequency dispersion processes (Figure 12).

Figure 14 illustrates $M_n^{'}$ plotted against the CEC to explore the relationship between chargeability and CEC. According to the model proposed by Revil et al. (2017), chargeability is expected to positively correlate with CEC and VWC, assuming that relaxation processes in this frequency range predominantly originate from double-layer interactions.

Figure 10. Effective relative permittivity $\varepsilon_{r,eff}^{\star}(f)$ of the four clay materials at $f = 1$ MHz (left) and $f = 10$ MHz (right) as a function of the Cation Exchange Capacity. The respective boxplots, with additional mean values ($\cdot$), show the statistics of all measurements for each clay type.

However, since different relaxation effects overlap in the middle and lower frequency ranges, and the apparent chargeability is an extrapolated parameter, a clear dependence of chargeability on the CEC cannot be established unequivocally. Consequently, no definitive correlation is observed in Figure 14.

4.4. Mixture Models

The spectra of soils with high clay content can only partially be described by the CRIM mixture approach, as shown in Figure 15. Above 400 MHz, the model provides a good estimation of the amount of free pore water by
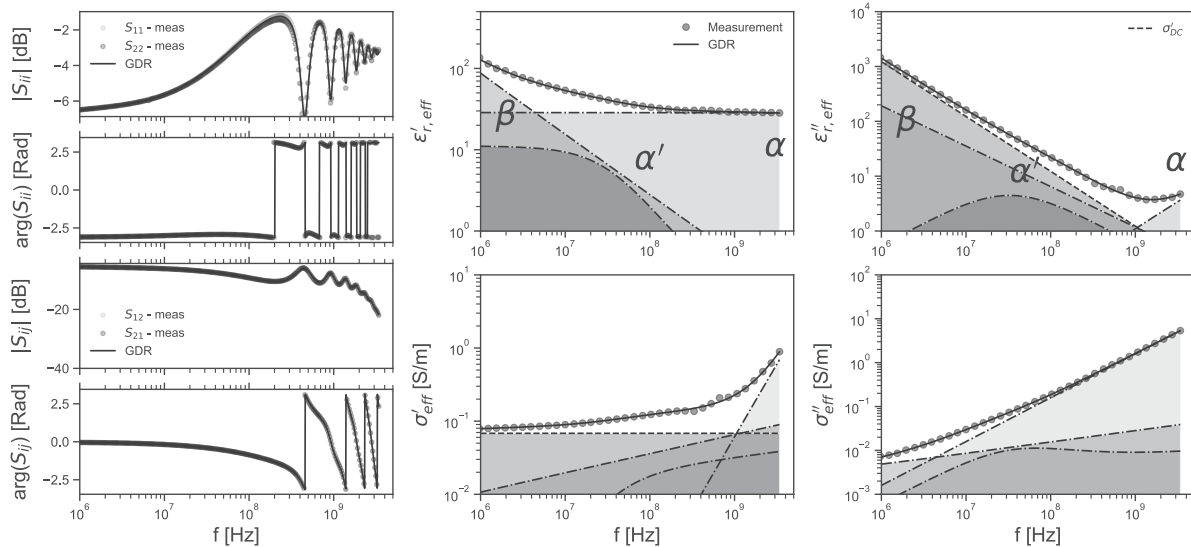

Figure 11. Measured and modeled (GDR, generalized dielectric response) HF-EM material properties of kaolin sample ID602 over frequency. Left: S-parameter. Center: complex effective relative permittivity. The HF-water relaxation contribution is depicted by α. The other terms are α' for the intermediate and β for the low-frequency relaxation processes. Right: complex effective electrical conductivity.
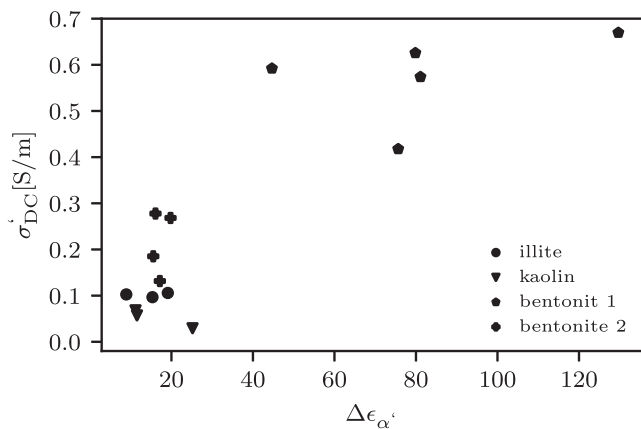
Figure 12. Relaxation strength of the second relaxation process versus direct current conductivity σ'_{DC} in the GDR model.

accurately modeling $\varepsilon'_{r,eff}$. Although the direct current conductivity aligns reasonably well with the measurements, the CRIM approach fails to adequately capture low-frequency dispersion, limiting its applicability for characterizing dielectric behavior in this range.

The ABC-M approach (Figure 16) demonstrates greater flexibility for characterizing the full spectrum due to the inclusion of an additional relaxation term. This flexibility allows the ABC-M to better represent both high- and low-frequency behavior compared to the CRIM approach. However, the physical interpretation of the exponents m and n in the mixture term (see Figure 17) requires further investigation. These parameters are highly sensitive to variations in water saturation and porosity, which strongly influence the relationship between VWC θ and the relative permittivity at high frequencies, particularly $\varepsilon_{1\,GHz}$.

The CRIM model effectively captures high-frequency behavior above 400 MHz, where water content and porosity dominate the dielectric response. However, it underrepresents the influence of CEC and associated low-frequency dispersion effects, highlighting the importance of more advanced models for clays with high CEC and porosity (Figure 15).

5. Discussion

The GDR, CPCM, and ABC-M models successfully replicate the broadband relaxation behavior of water-saturated clays over the investigated frequency range (Figures 11, 13, 15, 16). In contrast, the CRIM model accurately fits the high-frequency (HF, $f \geq 100$ MHz) real part of the complex effective permittivity and the low-frequency (LF, $f \leq 100$ MHz) imaginary part, but it does not adequately model dispersion phenomena. CPCM and GDR are purely phenomenological relaxation models, allowing for the comparison of individual relaxation processes. Meanwhile, ABC-M combines the strengths of a mixture equation with the adaptability of a relaxation model, enabling the decomposition of dispersion into distinct superimposed relaxation phenomena, which can be attributed to different physical causes.

While these approaches were primarily assessed in terms of physical interpretability and consistency with measured data, formal statistical model selection criteria such as the Akaike Information Criterion (AIC) or the Bayesian Information Criterion (BIC) could provide an additional quantitative framework for comparing the
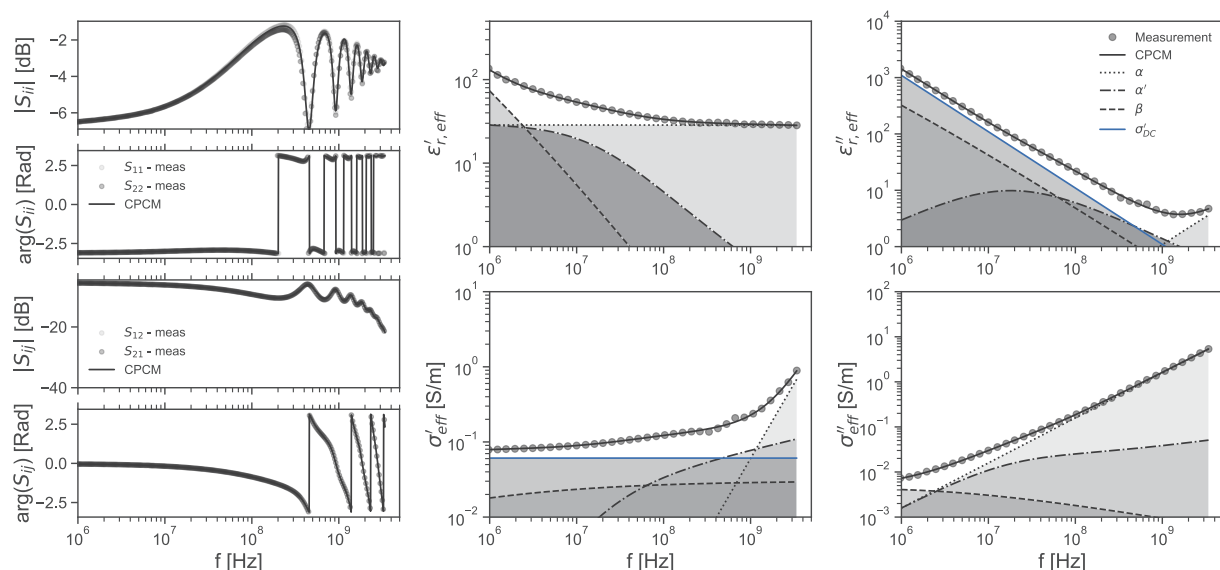

Figure 13. Measured and modeled Combined Permittivity and Conductivity Model HF-EM material properties of kaolin sample ID602 over frequency. Left: S-parameter. Center: complex effective relative permittivity.
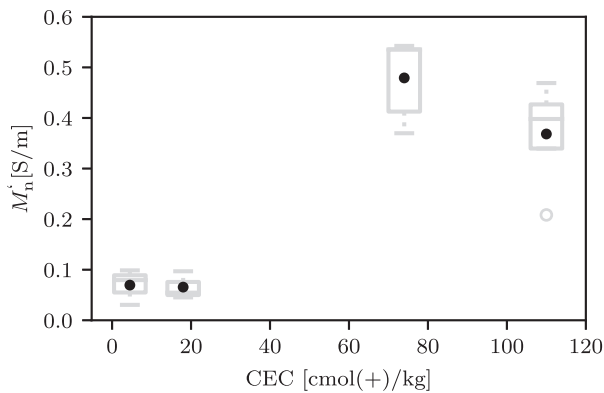
Figure 14. Normalized apparent chargeability M'_n of the third relaxation process in the Combined Permittivity and Conductivity Model as a function of the Cation Exchange Capacity.

performance of the different inversion approaches. These criteria balance model fit with the number of free parameters and could therefore complement the physical reasoning applied here. A systematic application of such criteria would require additional work beyond the scope of this study but represents a promising direction for future investigations.

These results align with the central hypothesis of this study, CEC, VWC, and porosity are significant factors influencing the dielectric properties of water-saturated clays. The modeling approaches and experimental analyses confirm the relevance of these physicochemical parameters, emphasizing the validity of the chosen methodology.

A detailed comparison of the inversion results (Figure 17) reveals that the models produce partially consistent results in frequency ranges dominated by specific relaxation phenomena, such as water relaxation.

5.1. Water Relaxation

One parameter consistent across all three models is the position of the free water relaxation peak, which is precisely determined despite the restricted frequency window with a maximum of 5 GHz. For all models and clay types, the relaxation time is observed between 5 and 9 ps, corresponding to relaxation frequencies between 32 and 18 GHz, aligning well with values reported in Kaatze (2007). The mean value for kaolin, 6.3 ps (25 GHz), is slightly lower than that of the other clays, which average 7.9 ps (20 GHz).

In the CPCM and GDR models, additional parameters of the water Debye term, ε_{inf} and $\Delta\varepsilon_{1,\alpha}$, are also inverted. Both models yield nearly identical values for the high-frequency limit (≈ 5), consistent with literature values for pure water (Kaatze, 2007). Furthermore, the relaxation strength demonstrates a positive correlation with the VWC, as expected. A higher VWC contributes more significantly to the overall polarizability.

5.2. Intermediate Relaxation

The intermediate relaxation process, situated between the RF water relaxation and the LF process, is modeled in both the GDR and CPCM approaches using a Cole-Cole term. Therefore, the results are expected to be at least partially comparable. Regarding the relaxation peaks $\tau_{2,\alpha'}$, the CPCM estimates range from 1.1 to 8.8 ns
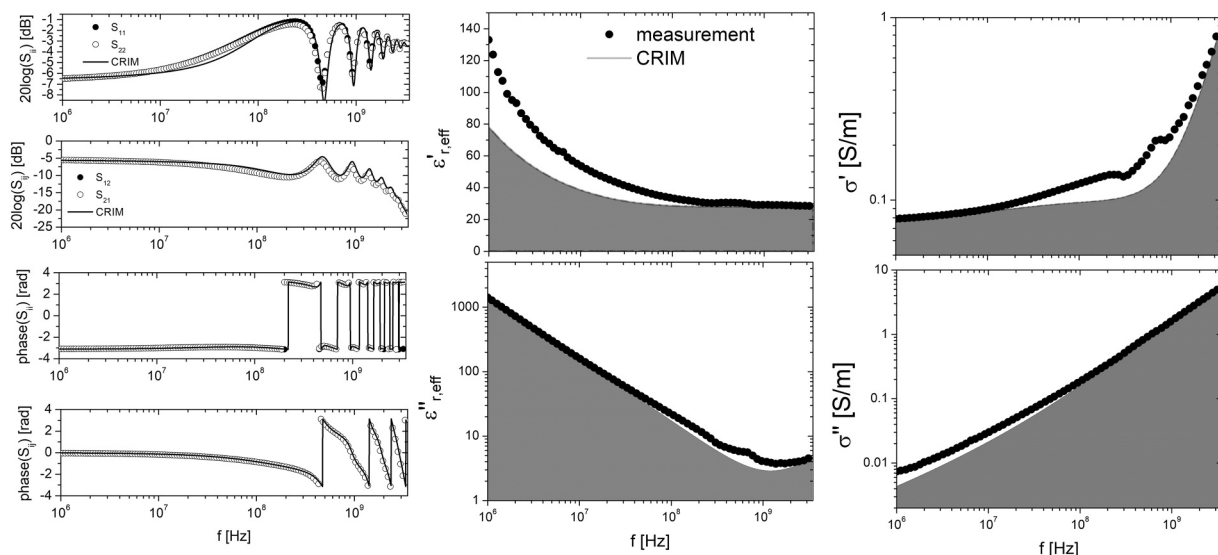

Figure 15. Measured and modeled (CRIM–Complex Refractive Index Model) HF-EM material properties of kaolin sample ID602 over frequency. Left: S-parameter. Center: complex effective relative permittivity. Right: complex effective electrical conductivity.

Figure 16. Measured and modeled (ABC-M, Augmented Broadband Complex Dielectric Mixture Model) HF-EM material properties of kaolin sample ID602 over frequency. Left: S-parameter. Center: complex effective relative permittivity. Right: complex effective electrical conductivity.
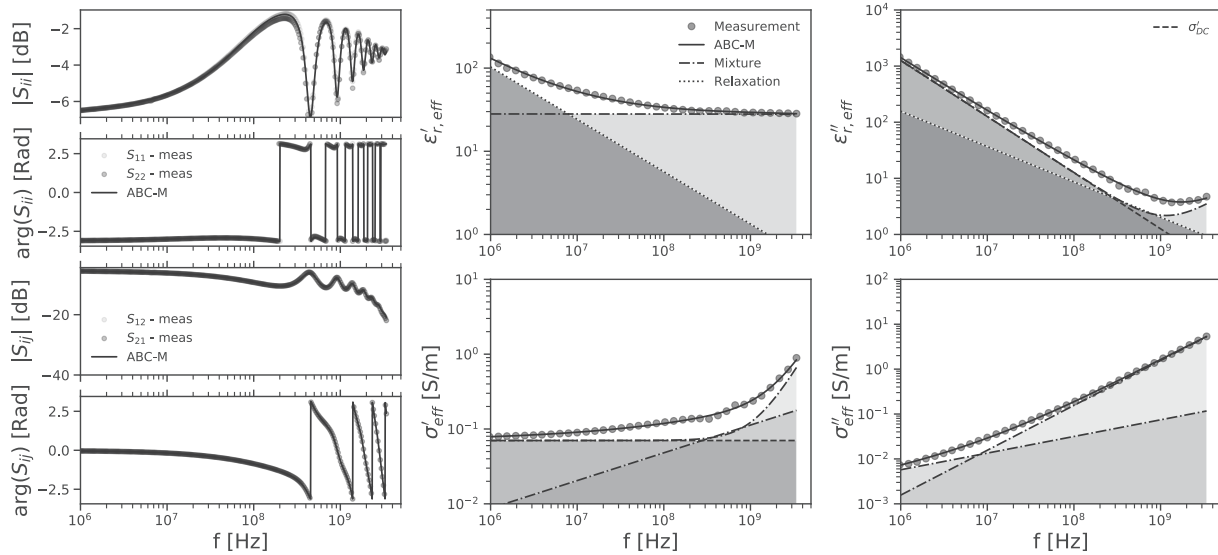
(145–18 MHz), while the GDR values span from 1.1 to 71 ns (145–2 MHz). All observed values thus fall within the MHz range. The CPCM inversion values for kaolin stand out, with an average relaxation time of 8.3 ns (19 MHz), significantly higher than the average of the other clays at 2.1 ns (76 MHz). This deviation warrants further investigation, particularly concerning the microscopic clay structure.

The relaxation strengths, $\Delta\varepsilon_2$, estimated by the CPCM range from $18 \leq \Delta\varepsilon_2 \leq 33$, which aligns closely with the GDR estimates of $9 \leq \Delta\varepsilon_{\alpha\prime} \leq 25$. A slight positive correlation between relaxation strength and relaxation time is observed, largely attributed to the pronounced $1/\log(f)$ dependence of the imaginary part $\varepsilon''_{r,\text{eff}}$ in this frequency range. Interestingly, the GDR results for bentonite 1 show substantially higher relaxation strengths of $45 \leq \Delta\varepsilon_{\alpha\prime} \leq 130$, likely due to the stronger soda activation.

The observed relationship between CEC and relaxation strength, particularly for bentonite 1, underscores the critical role of CEC in determining low-frequency dispersion processes. This finding highlights the potential of these models to serve as diagnostic tools for quantifying CEC indirectly through dielectric measurements. Since conductivity effects are particularly relevant in this frequency range, we now report the intermediate relaxation parameters both in absolute terms and normalized to the measured DC conductivity. This normalization allows a clearer comparison across clay types with different ionic strengths and also facilitates comparison with the LF relaxation process, where similar considerations apply.

5.3. Low-Frequency Relaxation

In the lower frequency range, the relaxation process dominates the overall frequency dependence of $\varepsilon'_{r,\text{eff}}$. Therefore, any broadband relaxation model or mixture equation must incorporate this process to accurately reflect its significant contribution. The approaches used here—GDR, CPCM, and ABC-M—each include a relaxation term (referred to as the third process) to model this behavior. In contrast, CRIM accounts for this dispersion implicitly through the structural exponent 0.5 (Wagner et al., 2011). While GDR and ABC-M use formulations within the permittivity domain, CPCM employs a conductivity representation. All three models accurately predict the low-frequency dispersion, whereas in CRIM, the structural exponent must be adjusted to reflect particle size distribution and particle orientation in the applied electrical field (Jones & Friedman, 2000; Sihvola, 2000; Wagner et al., 2011). These differing modeling domains lead to variations in parameter estimates for describing the dispersion. Since DC conductivity strongly contributes to both LF and intermediate relaxation processes, it is essential to report not only the normalized response but also to explicitly account for conductivity effects in the modeling. Conductivity influences not only the imaginary part of the permittivity spectrum via amplitude, but also the real part through frequency shifting, and should therefore be consistently incorporated in future model developments.
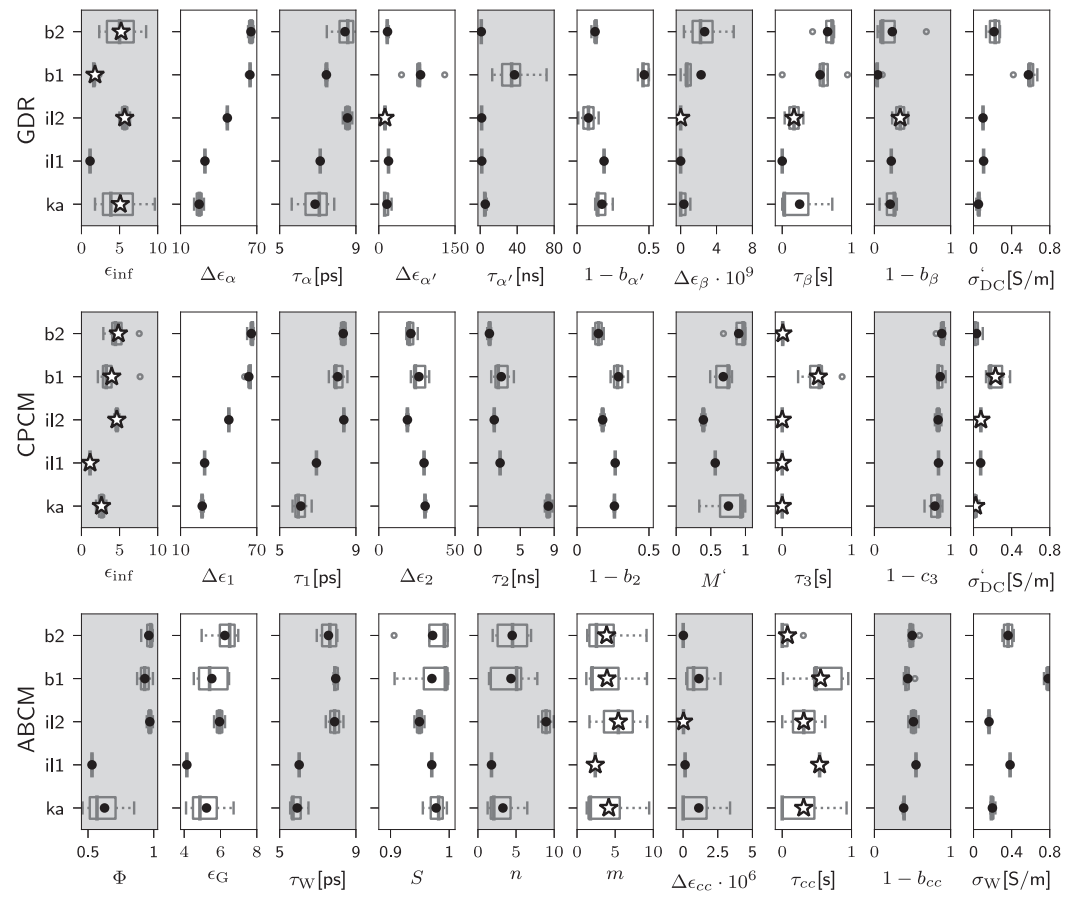
Figure 17. Results of the inverse parameter estimation for three models: Fractional Dielectric Relaxation Model (GDR), Combined Permittivity and Conductivity Model (CPCM), and Augmented Broadband Complex Dielectric Mixture Model (ABC-M). For each clay type (ka - kaolin, il1 - illite 1, il2 - illite 2, b1 - bentonite 1, b2 - bentonite 2), the set statistics are represented by a boxplot for each parameter individually. Additionally, the mean is depicted by a ·; or by a @@@[.6] if the inversion parameters have an uncertainty greater than 10% of the parameter value.

While the models effectively capture broadband dielectric behavior, certain limitations remain. For instance, the CRIM model struggles with low-frequency dispersion, and the ABC-M model requires further refinement to decouple correlated parameters like porosity and solid particle permittivity. The interpretation of ε_G should,

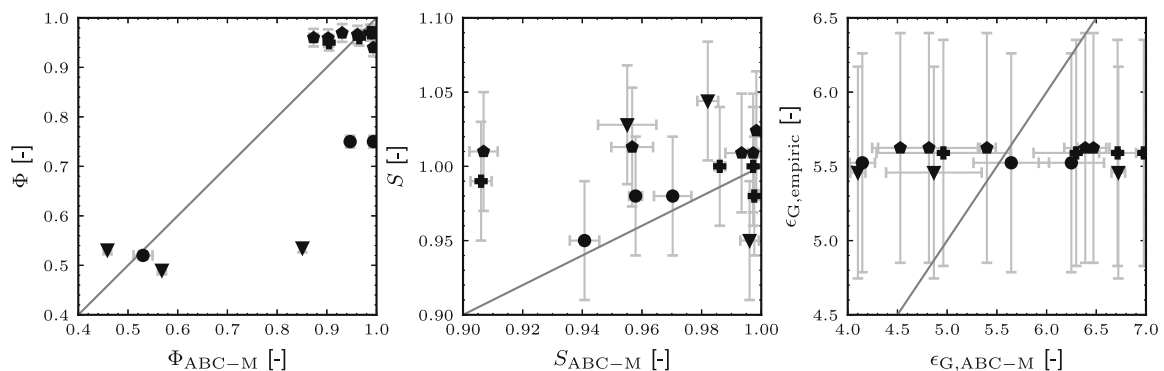**Figure 18.** Comparison of ABC-M model-inverted parameters: porosity ϕ, water saturation S, and permittivity of the solid particles ε_G with measurements by other methods. Gray uncertainty bars are included, and the diagonal line represents a 1:1 correlation.

however, be treated with caution. While conservative estimates often assume values around 5.5, clay particles do not exist as isolated mineral phases. Instead, they represent anisotropic, charged entities surrounded by electrical double layers, hydrated ions, and bound water. Thus, the "solid particle permittivity" is better understood as an effective property of this composite particle-plus-double-layer system rather than of the pure mineral lattice alone, although it remains a useful parameterization target. Future work could focus on extending the frequency range of measurements or incorporating additional physical constraints to enhance model accuracy.

For parameters such as $1 - b_\beta$, $1 - c_3$, and $1 - b_{cc}$, which define the width and shape of the relaxation peak, the results are consistent within each model but exhibit significant differences across models. Similarly, the position of the relaxation peak on the frequency axis, characterized by the relaxation time τ, does not yield consistently similar values across models. Notably, a strong parameter uncertainty, highlighted by @@@[.6], is observed. This is expected, as the relaxation frequencies and magnitudes of the assumed processes lie outside the measured frequency window.

This study contributes to the growing body of knowledge on dielectric spectroscopy by providing a comprehensive analysis of multiple modeling approaches. By correlating dielectric parameters with CEC, water content, and porosity, the findings bridge experimental observations with theoretical predictions, offering a robust framework for future research in soil and material sciences.

Furthermore, the relaxation phenomena in the lower frequency range—such as double-layer relaxation, counter-ion relaxation, and the Maxwell-Wagner effect—exhibit a strong dependence on geometry and are often superimposed. The complex pore and particle shapes result in numerous possible frequency dependencies, leading to a broad and smooth relaxation signature (Wagner et al., 2011). Relaxation strengths, $\Delta\varepsilon_\beta$, M', and $\Delta\varepsilon_{cc}$, vary significantly across models, underscoring the influence of model formulations. This suggests that combining theoretical mixture equations with flexible relaxation terms, such as Cole-Cole-type functions, could more effectively connect the HF and LF ranges.

The ability of the models to accurately represent relaxation processes has both scientific and practical implications. For example, these findings can be applied in geotechnical engineering and soil science to better evaluate the mechanical and hydraulic properties of soils. Moreover, these models could assist in optimizing industrial processes that rely on the understanding of clay-water interactions, such as drilling fluid design or soil stabilization techniques.

5.4. DC Conductivities

The conductivity values, shown on the far-right side of Figure 17, are in a similar range across all three models. However, the pore water conductivity is somewhat higher for ABC-M compared to CRIM. This difference is plausible, as the pore water conductivity in ABC-M is treated separately, while the apparent DC conductivities also account for surface conductivity contributions, as described by the modified Archie model (Revil et al., 2007). It should be emphasized that the pore water conductivity is a measurable parameter that can be determined independently by extracting the pore solution and measuring its conductivity with a four-electrode cell at low frequencies (hundreds of Hz to a few kHz). This provides a reliable approximation of the DC conductivity of the equilibrium pore water. To clarify this link, we have compared the directly measured pore water conductivities (see Table 3) with the values estimated by the models. While the absolute values show good agreement in most cases, systematic deviations remain for bentonite 1 due to its oversupply of free ions. This explicit comparison underlines the need to distinguish clearly between directly measurable pore water conductivities and the apparent DC conductivities derived from dielectric models:

$$\sigma_{eff}^\star = \frac{\sigma_w^\star}{F} + \left(1 - \frac{1}{F}\right)\sigma_S^\star \tag{17}$$

The variable $\sigma_w^\star$ is the complex conductivity of the aqueous pore solution, $\sigma_S^\star$ is the complex surface conductivity, and $F = \phi^{-m}$ is the formation factor, which relates to porosity ϕ using the cementation exponent m. The complex pore water conductivity, $\sigma_w^\star$, is modeled using the approach by Jougnot et al. (2010):

$$\sigma_w^\star = j\omega\varepsilon_0\varepsilon_{r,W}^\star \tag{18}$$

Here, $\varepsilon_{r,W}^{\star}$ is the relative complex permittivity of the aqueous pore solution, derived from Equation 8, including σ_w. In this formulation, the true pore water conductivity σ_W enters explicitly via the imaginary part of $\varepsilon_{r,W}^{\star}$, that is, through the term $-j\sigma_W/(\omega\varepsilon_0)$. Thus, Equation 18 consistently accounts for both the dielectric and conductive contributions of the pore water. As discussed earlier, bentonite 1 deviates from these conductivity values due to its strong sodium carbonate activation.

A noticeable difference is observed in the σ'_{DC} values between the GDR and CPCM models. The CPCM-derived values are systematically lower than those of GDR. This discrepancy arises because these conductivities are apparent DC conductivities extracted from RF measurements rather than measured directly. Additionally, in CPCM, σ'_{DC} becomes frequency-dependent through the third relaxation term (see Equation 3), resulting in slightly lower values. This frequency dependence can be considered a conceptual weakness of the CPCM, as it removes a parameter that is otherwise directly measurable and should ideally remain independent within the model framework. Keeping measurable quantities such as the pore water conductivity as external constraints improves model robustness and facilitates a clearer comparison between measured and modeled values. The relaxation frequency of the conductivity process in CPCM is constrained to frequencies above 10 MHz, making the model more suitable for measurements that include spectroscopic data from the kHz range. However, the apparent chargeability $M' = \sum_k^N m_k$ obtained in CPCM, serves as a measure of the total polarization contribution, encompassing all superimposed processes.

The apparent conductivity of the aqueous pore solution, σ_W, derived from CRIM (Table 2) and ABC-M, as well as the apparent DC conductivities, σ'_{DC}, estimated by GDR and CPCM, exhibit a strong correlation with CEC. The correlation between DC conductivity and CEC observed across the models further emphasizes the relevance of CEC as a diagnostic parameter in soil science. By linking DC conductivity with clay-water interactions, this study highlights its potential as a proxy for assessing soil properties such as permeability and ionic mobility. This connection strengthens the practical applicability of the presented approaches for real-world geotechnical and environmental challenges. The chosen setup and models are directly transferable to in situ conditions, where the natural variability of water content, pore water conductivity, and degree of saturation provides an opportunity to test model robustness under realistic constraints.

Once again, bentonite 1 deviates from the expected relationship due to its high sodium carbonate activation. As CEC increases, more cations are present on the inner surfaces of clay mineral particles. These samples were saturated with deionized water, leading to higher concentrations of free charges in the aqueous pore solution and systematic variations in conductivity across all models. However, in bentonite 1, the excessive free ions in the suspension, which are not solely dissociated from the clay surface, disrupt this correlation. The appropriate volume fraction of water, as indicated in Table 2, mitigates this increase in ion concentration, reducing its impact on relaxation parameters, including direct current conductivity.

5.5. ABC-M Specific Parameters

Due to the formulation of the ABC-M mixture model, parameters such as porosity ϕ, permittivity of the solid particles ε_G, and saturation S can be estimated from the measured spectra by comparing them to the determined parameters (see Section 3). Unlike the CRIM inversion, where certain parameters are pre-determined, the ABC-M model leaves all parameters open, even when some are known. This flexibility allows for an assessment of the model's performance when analyzing completely unknown materials. The comparison of these measurements is shown in Figure 18.

As observed in Figure 18, the majority of the porosity values are well estimated by the ABC-M model. However, the presence of three outliers suggests a potential correlation with other parameters. Saturation values, which are close to 1, are also well predicted by the model. In the case of the permittivity of the solid particles ε_G, the values determined by the helium pycnometer and Equation 6 and 7 range between 4.5 and 5.0. However, the values estimated by ABC-M vary between 4 and 7, indicating that the model struggles to determine this parameter accurately. This discrepancy likely arises because ε_G is correlated with porosity and the cementation exponent m in the model. Consequently, incorporating a priori information to fix this parameter would improve the model's reliability.

The saturation exponent n and the cementation exponent m exhibit significant variation within their inversion bounds. For a single clay type, individual sample values often vary widely, with illite spanning nearly the entire boundary interval. This behavior is even more pronounced for m, which shows similar distributions across all four clay types. Such variability is expected since $S_W \approx 1$, rendering the saturation exponent n almost irrelevant to the modeled effective permittivity.

The ABC-M model's ability to estimate porosity and water saturation aligns well with the study's goal of linking dielectric behavior to fundamental soil parameters. However, the challenges in accurately determining the permittivity of solid particles highlight the need for incorporating external constraints or more precise parameterizations in future work. However, the challenges in accurately determining the permittivity of solid particles highlight the need for incorporating external constraints, more precise parameterizations, or additional training on extended sample sets in future work. These refinements could enhance the robustness of ABC-M for broader applications in soil characterization and material design.

In addition to the phenomenological and stretched-relaxation models tested here, classical mixture-theory approaches have been widely applied in related contexts (e.g., T. Han et al., 2018). Such models offer a complementary framework and enable direct comparisons between "stretched relaxation" and "mixture" descriptions. Another promising avenue is the use of Relaxation Time Distribution (RTD) analysis, as proposed by Connolly et al. (2019), which, although rarely applied in the high-frequency soil science community, could be particularly powerful when combined with time-lapse measurements. Finally, extending the present work to more realistic geomaterials such as compacted bentonites (e.g., Beloborodov et al., 2017) would provide additional relevance for natural systems.

In cases of near saturation, the ABC-M mixture term must be reduced to the following form, as described in Bore et al. (2018):

$$\varepsilon^{\star}_{\mathrm{r,\ VA}} = \phi^m \left[\varepsilon^{\star}_{\mathrm{r,W}} + (\phi^{-m} - 1)\varepsilon_{\mathrm{G}} \right] \tag{19}$$

Here, $\varepsilon^{\star}_{\mathrm{r,W}}$ represents the complex relative permittivity of water and ε_{G} corresponds to the permittivity of the solid particles. This reduced form highlights the diminishing influence of n under saturated conditions and emphasizes the need for accurate parameterization of ϕ, ε_{G}, and m.

5.6. Limitations and Outlook

This study is based on a limited set of representative clay samples and therefore provides an illustrative rather than a parametric exploration of broadband dielectric spectroscopy. Systematic investigations with larger sample series, including controlled variations in water content, pore-water salinity, and mineral mixtures, are essential to fully assess the predictive power of the method. Such studies are beyond the scope of the present work but represent a clear direction for future research.

6. Conclusion

In this study, the dielectric spectra of four different water-saturated clays were analyzed in the frequency range from 1 MHz to 5 GHz. The investigation employed direct spectrum analysis, semi-empirical and theoretical mixture models, as well as phenomenological relaxation functions to explore the relationships between dielectric properties and clay-specific parameters.

One central hypothesis of this study was that the mineralogical composition of water-saturated clays significantly influences their high-frequency electromagnetic response. This, in turn, would allow material-specific parameters, such as the CEC, to be extracted from broadband dielectric spectra. The results indicate that this hypothesis holds qualitatively true for most cases, with some notable exceptions.

By directly analyzing permittivity and conductivity spectra, qualitative correlations with clay-specific parameters were observed. For instance, the real parts of the spectra at 10 MHz demonstrated a positive correlation with CEC. The influence of the SSA, particularly the electrostatic double layer, was found to dominate over geometric effects, such as the Maxwell-Wagner polarization. This supports the observation that permittivity correlates more

strongly with CEC and SSA. On the other hand, the imaginary part at 10 MHz was shown to depend heavily on the conductivity of the material.

These observations underscore the importance of clay-specific surface properties, such as the electrostatic double layer, in influencing dielectric parameters. The differentiation of relaxation phenomena also highlights the challenges of disentangling overlapping processes in complex geomaterials, necessitating further refinement of analytical and modeling techniques.

In addition, the findings emphasize the relevance of dielectric spectroscopy as a non-invasive tool to link electromagnetic responses to specific properties such as CEC, porosity, and water content. This study advances the understanding of how mineralogical composition and ion exchange processes in clays govern their broadband dielectric behavior, providing a foundation for practical subsurface characterization methods in geophysical and geotechnical applications.

This behavior was consistent across naturally occurring clays like kaolin, illite, and bentonite 2. However, the strongly soda-activated bentonite 1 deviated from expectations, demonstrating that chemical treatments significantly impact the dielectric spectra.

Quantitative estimations using adjusted models such as ABC-M and CPCM proved challenging due to overlapping relaxation phenomena within this frequency range, which could not be fully disentangled. Additionally, models that integrate dielectric properties with chemical parameters, such as CEC, rely on low-frequency measurements, resulting in inaccuracies when extrapolated to the high-frequency range.

By integrating experimental data with advanced modeling approaches such as GDR, CPCM, and ABC-M, this research contributes to bridging the gap between fundamental mineral physics and applied electromagnetic methods. The ability of these models to predict material properties with high accuracy highlights their potential for broader applications in field-scale geophysical monitoring.

The three models—Generalized Dielectric Relaxation Model (GDR), Combined Permittivity and Conductivity Model (CPCM), and Augmented Broadband Complex Dielectric Mixture Model (ABC-M)—successfully predicted the broadband dielectric spectra of the materials with high accuracy. However, the Complex Refractive Index Model (CRIM) was less effective at accounting for strong relaxation processes below 400 MHz. Furthermore, this study confirmed that water content determination of clayey geomaterials using permittivity measurements can only be approximate when applying the Topp formula.

While the investigated models show great promise, particularly in the RF range, limitations in capturing low-frequency dispersion (e.g., in the CRIM model) underline the need for combining broadband dielectric methods with complementary low-frequency techniques, such as SIP. Such combinations could improve parameter estimation for critical subsurface properties, including those in highly saline or organic-rich environments.

This study highlights promising correlations between dielectric measurements and clay mineral parameters. It demonstrates that ion exchange processes at clay surfaces significantly influence the dielectric spectrum in the RF range, enabling qualitative material property assessments. For instance, spatial heterogeneities in nutrient uptake capacity on agricultural fields could potentially be mapped. Additionally, in borehole applications, relationships between dielectric measurements and geomaterial parameters are already being utilized in industrial practices.

To deepen these insights, future research should include systematic variations in water content, porosity, and pore water salinity. These variations could help refine and evaluate existing models. This difficulty also explains the limited data set in the present study, as swelling clays cannot easily be prepared in homogeneous equilibrium with either very fresh or highly saline pore water. However, experimental handling of highly swelling clays poses significant challenges and necessitates novel measurement and geotechnical techniques. Combining these methods with low-frequency approaches, such as SIP or Complex Conductivity (CC), could enhance accuracy and provide further valuable insights.

Expanding the experimental scope to include real soils with varying OM content and salinity would enhance the understanding of their dielectric behavior. As a next step, future research should aim to extend these analyses to real soils that contain soil OM. Particularly in surface soils, OM commonly contributes the largest share to the total CEC, and its presence may significantly affect dielectric behavior. Addressing these influences would allow

a more comprehensive and realistic modeling of natural soil systems. Organic matter, which strongly influences CEC, presents additional challenges due to its heterogeneity. Addressing these complexities could significantly improve the applicability of dielectric methods in natural and engineered geomaterials. This study also demonstrated the reliability of models for describing the dielectric properties of clays and clay-rich materials, which are critical for applications such as GPR. Furthermore, the limitations of the Topp formula in estimating soil moisture content in clay-rich soils were highlighted. By leveraging the proposed models, improvements in accuracy can be achieved, particularly in estimating water-filled porosity, a crucial parameter for hydrological and petrophysical applications.

Overall, the integration of experimental, modeling, and theoretical insights in this study paves the way for the development of robust, scalable, and non-invasive soil monitoring tools. These tools hold significant promise for improving agricultural productivity, optimizing water resource management, and supporting climate resilience strategies in the face of global environmental challenges.

Conflict of Interest

The authors declare no conflicts of interest relevant to this study.

Data Availability Statement

The broadband dielectric spectroscopy data and measured sample properties used in this study are openly available. The dataset includes scattering parameter files (.s2p) and measured mineralogical and petrophysical data. The data are available under Schmidt et al. (2025).

References

Adão, F., Pádua, L., & Sousa, J. J. (2025). Evaluating soil degradation in agricultural soil with ground-penetrating radar: A systematic review of applications and challenges. *Agriculture*, *15*(8). https://doi.org/10.3390/agriculture15080852

Arcone, S., Grant, S., Boitnott, G., & Bostick, B. (2008). Complex permittivity and clay mineralogy of grain-size fractions in a wet silt soil. *Geophysics*, *73*(3), J1–J13. https://doi.org/10.1190/1.2890776

Asano, M., Sudo, S., Shinyashiki, N., Yagihara, S., Ohe, T., Morimoto, N., & Fujita, K. (2007). Studies of dielectric properties of bentonite obtained by broadband dielectric spectroscopy. In S. Okamura (Ed.), *7th international conference on electromagnetic wave interaction with water and moist substances, ISEMA* (pp. 25–30).

Assifaoui, A., Moussa, R., & Blanchart, P. (2001). Dielectric dispersion in the frequency range 1 MHz - 1 GHz of concentrated suspensions in relation to rheology. *Journal of Colloid and Interface Science*, *244*(1), 74–78. https://doi.org/10.1006/jcis.2001.7904

ASTM. (2009). Standard test methods for laboratory compaction characteristics of soil using standard effort (technical report).

Beloborodov, R., Pervukhina, M., Han, T., & Josh, M. (2017). Experimental characterization of dielectric properties in fluid saturated artificial shales. *Geofluids*, *2017*(1), 1019461. https://doi.org/10.1155/2017/1019461

Benavides, J., Myers, M., & Hathon, L. (2023). Dielectric response interpretation of source rocks. In *SPE/AAPG/SEG unconventional resources technology conference 2023*. https://doi.org/10.15530/urtec-2023-3854429

Binley, A., & Slater, L. (2020). *Resistivity and induced polarization: Theory and applications to the near-surface Earth*. Cambridge University Press.

Bobrov, P., Belyaeva, T., Kroshka, E., & Rodionova, O. (2021). Dielectric spectroscopy of slightly saline sandy-clay mixtures in the frequency range from 10 kHz to 10 GHz. In *13th international conference on electromagnetic wave interaction with water and moist substances (ISEMA)* (pp. 1–6). https://doi.org/10.1109/ISEMA49699.2021.9508340

Boivin, A. L., Tsai, C., Hickson, D. C., Ghent, R. R., & Daly, M. G. (2022a). Determination of broadband complex EM parameters of powdered materials: 1. MCMC-Based two-port transmission line measurements. *Journal of Geophysical Research: Planets*, *127*(10), e2022JE007199. https://doi.org/10.1029/2022JE007199

Boivin, A. L., Tsai, C., Hickson, D. C., Ghent, R. R., & Daly, M. G. (2022b). Determination of broadband complex EM parameters of powdered materials: 2. Ilmenite-bearing lunar analogue materials. *Journal of Geophysical Research: Planets*, *127*(10), e2022JE007200. https://doi.org/10.1029/2022JE007200

Bona, N., Rossi, E., Venturini, C., Capaccioli, S., Lucchesi, M., & Rolla, P. A. (1998). Characterization of rock wettability though dielectric measurements. *Revue de l'Institut Français du Petrole*, *53*(6), 771–783. https://doi.org/10.2516/ogst:1998068

Bore, T., Coperey, A., Wagner, N., Mishra, P. N., Scheuermann, A., & Revil, A. (2022). Experimental determination of frequency-and temperature-dependent electrical properties of water-saturated clays using spectral induced polarization and network analyzer technique. *Measurement*, *190*, 110653. https://doi.org/10.1016/j.measurement.2021.110653

Bore, T., Mishra, P. N., Bialkowski, K., Grieve, S., Wagner, N., & Scheuermann, A. (2021). Multiple open ended probe for spatio-temporal dielectric spectroscopy: Application to evaporative dewatering. *Measurement*, *173*, 108521. https://doi.org/10.1016/j.measurement.2020.108521

Bore, T., Mishra, P. N., Wagner, N., Schwing, M., Honorio, T., Revil, A., & Scheuermann, A. (2021). Coupled hydraulic, mechanical and dielectric investigations on kaolin. *Engineering Geology*, *294*, 106352. https://doi.org/10.1016/j.enggeo.2021.106352

Bore, T., Schwing, M., Serna, M. L., Speer, J., Scheuermann, A., & Wagner, N. (2018). A new broadband dielectric model for simultaneous determination of water saturation and porosity. *IEEE Transactions on Geoscience and Remote Sensing*, *56*(8), 4702–4713. https://doi.org/10.1109/tgrs.2018.2835447

Bore, T., Shen, Y.-J., Serati, M., Pascal, Y., Al Kalbani, M., Scheuermann, A., et al. (2025). Coaxial method to investigate broadband dielectric properties of rocks over the 5 Hz to 3 GHz frequency range. *Journal of Rock Mechanics and Geotechnical Engineering*, *17*(11), 6837–6852. https://doi.org/10.1016/j.jrmge.2025.04.024

Bore, T., Wagner, N., Cai, C., & Scheuermann, A. (2016). Broadband electromagnetic analysis of compacted kaolin. *Measurement Science and Technology*, *28*(1), 014016. https://doi.org/10.1088/1361-6501/28/1/014016

Bore, T., Wagner, N., Coperey, A., Loewer, M., Revil, A., & Scheuermann, A. (2021). Analysis of interfacial water in clay by high frequency dielectric relaxation spectroscopy. In *13th international conference on electromagnetic wave interaction with water and moist substances, ISEMA* (pp. 1–5). https://doi.org/10.1109/ISEMA49699.2021.9508278

Bore, T., Yan, G., Narayan Mishra, P., Brierre, T., Placencia-Gómez, E., Revil, A., & Wagner, N. (2024). A flow through coaxial cell to investigate high frequency broadband complex permittivity: Design, calibration and validation. *Measurement*, *237*, 115198. https://doi.org/10.1016/j.measurement.2024.115198

Bourg, I. C., & Sposito, G. (2011). Molecular dynamics simulations of the electrical double layer on smectite surfaces contacting concentrated mixed electrolyte (Nacl-Cacl$_2$) solutions. *Journal of Colloid and Interface Science*, *360*(2), 701–715. https://doi.org/10.1016/j.jcis.2011.04.063

Bourg, I. C., Sposito, G., & Bourg, A. C. M. (2007). Modeling the acid–base surface chemistry of montmorillonite. *Journal of Colloid and Interface Science*, *312*(2), 297–310. https://doi.org/10.1016/j.jcis.2007.03.062

Buchner, R., Barthel, J., & Stauber, J. (1999). The dielectric relaxation of water between 0°C and 35°C. *Chemical Physics Letters*, *306*(1–2), 57–63. https://doi.org/10.1016/S0009-2614(99)00455-8

Bumberger, J., Mai, J., Schmidt, F., Lünenschloß, P., Wagner, N., & Toepfer, H. (2018). Spatial retrieval of broadband dielectric spectra. *Sensors*, *18*(9), 2780. https://doi.org/10.3390/s18092780

Campbell, B. A. (2002). *Radar remote sensing of planetary surfaces*. Cambridge University Press.

Cardinale, B. J., Duffy, J. E., Gonzalez, A., Hooper, D. U., Perrings, C., Venail, P., et al. (2012). Biodiversity loss and its impact on humanity. *Nature*, *486*(7401), 59–67. https://doi.org/10.1038/nature11148

Casotti, C., Revil, A., Ghorbani, A., Abdelfattah, M., Guerini, M., Hoblea, F., et al. (2025). Induced polarization applied to landslides. Part 1: Imaging hydraulic barriers. *Geophysical Journal International*, *242*(2), ggaf218. https://doi.org/10.1093/gji/ggaf218

Casotti, C., Revil, A., Johnson, T., Ménard, G., Su, Z., Qiang, S., et al. (2025). Induced polarization applied to landslides. Part 2: Anatomy and water content tomography of a mudflow. *Geophysical Journal International*, *242*(2), ggaf219. https://doi.org/10.1093/gji/ggaf219

Chang, L., Ge, H., Shen, Y., Huang, Z., & Zhang, Q. (2018). Study on the law of membrane efficiency of unsaturated shale and its application. *Geofluids*, *2018*(1), 2854958. https://doi.org/10.1155/2018/2854958

Chelidze, T., Guéguen, Y., & Ruffet, C. (1999). Electrical spectroscopy of porous rocks: A review - II. Experimental results and interpretation. *Geophysical Journal International*, *137*(1), 16–34. https://doi.org/10.1046/j.1365-246x.1999.00800.x

Chen, L.-F., Ong, C. K., Neo, C., Varadan, V. V., & Varadan, V. K. (2004). *Microwave electronics: Measurement and materials characterization*. John Wiley & Sons.

Chen, Y., & Or, D. (2006). Geometrical factors and interfacial processes affecting complex dielectric permittivity of partially saturated porous media. *Water Resources Research*, *42*(6). https://doi.org/10.1029/2005WR004744

Cole, K. S., & Cole, R. H. (1941). Dispersion and absorption in dielectrics dispersion and absorption in dielectrics I. Alternating current characteristics. *Journal of Chemical Physics*, *9*(4/41), 341–351. https://doi.org/10.1063/1.1750906

Connolly, P. R. J., Josh, M., O'Neill, K. T., Seltzer, S. J., Wigand, M. O., Clennell, M. B., et al. (2019). Dielectric polarization studies in partially saturated shale cores. *Journal of Geophysical Research: Solid Earth*, *124*(11), 10721–10734. https://doi.org/10.1029/2019JB018195

Cosenza, P., Camerlynck, C., & Tabbagh, A. (2003). Differential effective medium schemes for investigating the relationship between high-frequency relative dielectric permittivity and water content of soils. *Water Resources Research*, *39*(9). https://doi.org/10.1029/2002WR001774

Davidson, D. W., & Cole, R. H. (1951). Dielectric relaxation in glycerol, propylene glycol, and n-propanol. *Journal of Chemical Physics*, *19*(12), 1484–1490. https://doi.org/10.1063/1.1748105

Debye, P. (1941). *Polar molecules*. Dover Publications, Inc.

Delavernhe, L., Steudel, A., Darbha, G. K., Emmerich, T., Schuhmann, R., Wöll, C., et al. (2015). Influence of mineralogical and morphological properties on the cation exchange behavior of dioctahedral smectites. *Colloids and Surfaces A: Physicochemical and Engineering Aspects*, *481*, 591–599. https://doi.org/10.1016/j.colsurfa.2015.05.031

Döbelin, N., & Kleeberg, R. (2015). Profex: A graphical user interface for the Rietveld refinement program BGMN. *Journal of Applied Crystallography*, *48*. https://doi.org/10.1107/S1600576715014685

Dobson, M. C., Ulaby, F. T., Hallikainen, M. T., & El-Rayes, M. A. (1985). Microwave dielectric behavior of wet soil - Part II: Dielectric mixing models. *IEEE Transactions on Geoscience and Remote Sensing, GE-*, *23*(1), 35–46. https://doi.org/10.1109/TGRS.1985.289498

Ellis, D. V., & Singer, J. M. (2007). *Well logging for Earth scientists* (Vol. 692). Springer.

Friedman, S. P. (2005). Soil properties influencing apparent electrical conductivity: A review. *Computers and Electronics in Agriculture*, *46*(1–3), 45–70. https://doi.org/10.1016/j.compag.2004.11.001

Garrouch, A. A. (2018). Predicting the cation exchange capacity of reservoir rocks from complex dielectric permittivity measurements. *Geophysics*, *83*(1), MR1–MR14. https://doi.org/10.1190/geo2017-0035.1

Garrouch, A. A., & Sharma, M. M. (1994). The influence of clay content, salinity, stress, and wettability on the dielectric properties of brine-saturated rocks: 10 Hz to 10 MHz. *Geophysics*, *59*(6), 909–917. https://doi.org/10.1190/1.1443650

Gomiero, T. (2016). Soil degradation, land scarcity and food security: Reviewing a complex challenge. *Sustainability*, *8*(3), 281. https://doi.org/10.3390/su8030281

González-Teruel, J. D., Jones, S. B., Soto-Valles, F., Torres-Sánchez, R., Lebron, I., Friedman, S. P., & Robinson, D. A. (2020). Dielectric spectroscopy and application of mixing models describing dielectric dispersion in clay minerals and clayey soils. *Sensors*, *20*(22), 6678. https://doi.org/10.3390/s20226678

Guo, L., & Lin, H. (2016). Critical zone research and observatories: Current status and future perspectives. *Vadose Zone Journal*, *15*(9), 1–14. https://doi.org/10.2136/vzj2016.06.0050

Gupta, J., Liverman, D., Prodani, K., Aldunce, P., Bai, X., Broadgate, W., et al. (2023). Earth system justice needed to identify and live within Earth system boundaries. *Nature Sustainability*, *6*(6), 630–638. https://doi.org/10.1038/s41893-023-01064-1

Han, M., Cuadros, J., Suarez, C. A. P., Decoster, E., Faivre, O., Mosse, L., et al. (2012). Continous estimate of cation exchange capacity from log data: A new approach based on dielectric dispersion analysis. In *SPWLA 53rd annual logging symposium* (p. SPWLA-2012-101).

Han, T., Beloborodov, R., Pervukhina, M., Josh, M., Cui, Y., & Zhi, P. (2018). Theoretical modeling of dielectric properties of artificial shales. *Geofluids*, *2018*(1), 2973181. https://doi.org/10.1155/2018/2973181

Havriliak, S. J., & Havriliak, S. J. (1996). *Dielectric and mechanical relaxation in materials: Analysis, interpretation, and application to polymers*. Hanser.

Heimovaara, T. J., Huisman, J. A., Vrugt, J. A., & Bouten, W. (2004). Obtaining the spatial distribution of water content along a TDR probe using the SCEM-UA Bayesian inverse modeling scheme. *Vadose Zone Journal*, *3*(4), 1128–1145. https://doi.org/10.2136/vzj2004.1128

Hizem, M., Budan, H., Devillé, B., Faivre, O., Mossé, L., & Simon, M. (2008). Dielectric dispersion: A new wireline petrophysical measurement. In *SPE annual technical conference and exhibition, 2008*. https://doi.org/10.2118/116130-MS

Hoekstra, P., & Delaney, A. (1974). Dielectric properties of soils at uhf and microwave frequencies. *Journal of Geophysical Research*, *79*(11), 1699–1708. https://doi.org/10.1029/JB079i011p01699

Huisman, J. A., Hubbard, S. S., Redman, J. D., & Annan, A. P. (2003). Measuring soil water content with ground penetrating radar: A review. *Vadose Zone Journal*, *2*(4), 476–491. https://doi.org/10.2136/vzj2003.4760

Ishida, T., Kawase, M., Yagi, K., Yamakawa, J., & Fukada, K. (2003). Effects of the counterion on dielectric spectroscopy of a montmorillonite suspension over the frequency range 10^5–10^{10} Hz. *Journal of Colloid and Interface Science*, *268*(1), 121–126. https://doi.org/10.1016/S0021-9797(03)00688-X

Ishida, T., Makino, T., & Wang, C. (2000). Dielectric-relaxation spectroscopy of kaolinite, montmorillonite, allophane, and imogolite under moist conditions. *Clays and Clay Minerals*, *48*(1), 75–84. https://doi.org/10.1346/CCMN.2000.0480110

Jones, S. B., & Friedman, S. P. (2000). Particle shape effects on the effective permittivity of anisotropic or isotropic media consisting of aligned or randomly oriented ellipsoidal particles. *Water Resources Research*, *36*(10), 2821–2833. https://doi.org/10.1029/2000WR900198

Jonscher, A. K. (1996). *Dielectric relaxation in solids*. Chelsea Dielectrics Press.

Josh, M. (2014). Dielectric permittivity: A petrophysical parameter for shales. *Petrophysics*, *55*(4). SPWLA-2014-v55n4a5.

Josh, M., & Clennell, B. (2015). Broadband electrical properties of clays and shales: Comparative investigations of remolded and preserved samples. *Geophysics*, *80*(2), D129–D143. https://doi.org/10.1190/geo2013-0458.1

Josh, M., Clennell, B., & Cauchefert, M. (2016). Dielectric permittivity and anisotropy of intact multi-saturated organic shales. (p. SPWLA-2016-W).

Jougnot, D., Revil, A., Lu, N., & Wayllace, A. (2010). Transport properties of the callovo-oxfordian clay rock under partially saturated conditions. *Water Resources Research*, *46*(8), W08514. https://doi.org/10.1029/2009WR008552

Kaatze, U. (2007). Reference liquids for the calibration of dielectric sensors and measurement instruments. *Measurement Science and Technology*, *18*(4), 967–976. https://doi.org/10.1088/0957-0233/18/4/002

Kaufhold, S., Emmerich, K., Dohrmann, R., Steudel, A., & Ufer, K. (2013). Comparison of methods for distinguishing sodium carbonate activated from natural sodium bentonites. *Applied Clay Science*, *86*, 23–37. https://doi.org/10.1016/j.clay.2013.09.014

Kelleners, T. J., Robinson, D. A., Shouse, P. J., Ayars, J. E., & Skaggs, T. H. (2005). Frequency dependence of the complex permittivity and its impact on dielectric sensor calibration in soils. *Soil Science Society of America Journal*, *69*(1), 67–76. https://doi.org/10.2136/sssaj2005.0067a

Kerr, Y. H., Waldteufel, P., Wigneron, J.-P., Martinuzzi, J., Font, J., & Berger, M. (2001). Soil moisture retrieval from space: The soil moisture and ocean salinity (SMOS) mission. *IEEE Transactions on Geoscience and Remote Sensing*, *39*(8), 1729–1735. https://doi.org/10.1109/36.942551

Kessouri, P., Furman, A., Huisman, J. A., Martin, T., Mellage, A., Ntarlagiannis, D., et al. (2019). Induced polarization applied to biogeophysics: Recent advances and future prospects. *Near Surface Geophysics*, *17*(6), 595–621. https://doi.org/10.1002/nsg.12072

Kettridge, N., Comas, X., Baird, A., Slater, L., Strack, M., Thompson, D., et al. (2008). Ecohydrologically important subsurface structures in peatlands revealed by ground-penetrating radar and complex conductivity surveys. *Journal of Geophysical Research*, *113*(G4). https://doi.org/10.1029/2008JG000787

Keysight-Technologies. (2017). De-embedding and embedding s-parameter networks using a vector network analyzer (technical report).

Klotzsche, A., Jonard, F., Looms, M., van der Kruk, J., & Huisman, J. (2018). Measuring soil water content with ground penetrating radar: A decade of progress. *Vadose Zone Journal*, *17*(1), 1–9. https://doi.org/10.2136/vzj2018.03.0052

Kohlrausch, R. (1847). Ueber das Dellmann'sche Elektrometer. *Annalen der Physik*, *12*(11), 353–393. https://doi.org/10.1002/andp.18471481102

Lauer, K., Wagner, N., & Felix-Henningsen, P. (2012). A new technique for measuring broadband dielectric spectra of undisturbed soil samples. *European Journal of Soil Science*, *63*(2), 224–238. https://doi.org/10.1111/j.1365-2389.2012.01431.x

Leroy, P., Maineult, A., Mendieta, A., & Jougnot, D. (2025). A mechanistic model for the complex conductivity of clay materials. I. Theory. *Geophysical Journal International*, *241*(1), 86–109. https://doi.org/10.1093/gji/ggae411

Leroy, P., & Revil, A. (2004). A triple-layer model of the surface electrochemical properties of clay minerals. *Journal of Colloid and Interface Science*, *270*(2), 371–380. https://doi.org/10.1016/j.jcis.2003.08.007

Linde, N., Binley, A., Tryggvason, A., Pedersen, L. B., & Revil, A. (2006). Improved hydrogeophysical characterization using joint inversion of cross-hole electrical resistance and ground-penetrating radar traveltime data. *Water Resources Research*, *42*(12). https://doi.org/10.1029/2006WR005131

Loewer, M., Günther, T., Igel, J., Kruschwitz, S., Martin, T., & Wagner, N. (2017). Ultra-broad-band electrical spectroscopy of soils and sediments - A combined permittivity and conductivity model. *Geophysical Journal International*, *210*(3), 1360–1373. https://doi.org/10.1093/gji/ggx242

Maineult, A., Leroy, P., Mendieta, A., & Jougnot, D. (2025). A mechanistic model for the complex conductivity of clay materials. II. Comparison to experimental data. *Geophysical Journal International*, *241*(1), 110–132. https://doi.org/10.1093/gji/ggae428

McLachlan, P., Karloukovski, V., & Binley, A. (2024). Field-based estimation of cation exchange capacity using induced polarization methods. *Earth Surface Processes and Landforms*, *49*(15), 4928–4944. https://doi.org/10.1002/esp.6004

McLachlan, P., Schmutz, M., Cavailhes, J., & Hubbard, S. (2022). Estimating grapevine-relevant physicochemical soil zones using apparent electrical conductivity and in-phase data from EMI methods. *Geoderma*, *426*, 116033. https://doi.org/10.1016/j.geoderma.2022.116033

Meaney, P. M., Gregory, A. P., Epstein, N. R., & Paulsen, K. D. (2014). Microwave open-ended coaxial dielectric probe: Interpretation of the sensing volume re-visited. *BMC Medical Physics*, *14*(1), 3. https://doi.org/10.1186/1756-6649-14-3

Meier, L. P., & Kahr, G. (1999). Determination of the cation exchange capacity (CEC) of clay minerals using the complexes of copper(II) ion with triethylenetetramine and tetraethylenepentamine. *Clays and Clay Minerals*, *47*(3), 386–388. https://doi.org/10.1346/CCMN.1999.0470315

Mendoza Veirana, G. M., Grison, H., Verhegge, J., Cornelis, W., & De Smedt, P. (2025). Exploring the link between cation exchange capacity and magnetic susceptibility. *Soil*, *11*(2), 629–637. https://doi.org/10.5194/soil-11-629-2025

Mitchell, J. K., & Soga, K. (2005). *Fundamentals of soil behavior* (3rd ed.). John Wiley & Sons. https://doi.org/10.1002/0471463027

Olhoeft, G. R. (1981). Electrical properties of rocks. In *Physical properties of rocks and minerals* (pp. 257–330). McGraw-Hill.

Peplinski, N. R., Ulaby, F. T., & Dobson, M. C. (1995). Dielectric properties of soils in the 0.3-1.3-GHz range. *IEEE Transactions on Geoscience and Remote Sensing*, *33*(3), 803–807. https://doi.org/10.1109/36.387598

Pirrone, M., Han, M., Bona, N., Borghi, M., Galli, M. T., Pampuri, F., et al. (2011). A novel approach based on dielectric dispersion measurements to evaluate the quality of complex shaly-sand reservoirs. *SPE Annual Technical Conference and Exhibition*, *2011*, SPE-147245-MS. https://doi.org/10.2118/147245-MS

Pride, S. (1994). Governing equations for the coupled electromagnetics and acoustics of porous media. *Physical Review B: Condensed Matter*, *50*(21), 15678–15696. https://doi.org/10.1103/PhysRevB.50.15678

Revil, A. (2013). Effective conductivity and permittivity of unsaturated porous material in the frequency range 1mHz to 1GHz. *Water Resources Research*, *49*(1), 306–327. https://doi.org/10.1029/2012WR012700

Revil, A., Coperey, A., Shao, Z., Florsch, N., Fabricius, I. L., Deng, Y., et al. (2017). Complex conductivity of soils. *Water Resources Research*, *53*(8), 7121–7147. https://doi.org/10.1002/2017WR020655

Revil, A., Ghorbani, A., Jougnot, D., & Yven, B. (2023). Induced polarization of clay-rich materials - Part 1: The effect of desiccation. *Geophysics*, *88*(4), MR195–MR210. https://doi.org/10.1190/geo2022-0510.1

Revil, A., & Leroy, P. (2001). Hydroelectric coupling in a clayey material. *Geophysical Research Letters*, *28*(8), 1643–1646. https://doi.org/10.1029/2000GL012268

Revil, A., Linde, N., Cerepi, A., Jougnot, D., Matthäi, S., & Finsterle, S. (2007). Electrokinetic coupling in unsaturated porous media. *Journal of Colloid and Interface Science*, *313*(1), 315–327. https://doi.org/10.1016/j.jcis.2007.03.037

Revil, A., Qi, Y., Ghorbani, A., Coperey, A., Finizola, A., & Soueid Ahmed, T. (2019). Induced polarization of volcanic rocks. 3. Imaging clay cap properties in geothermal fields. *Geophysical Journal International*, *218*(2), 1398–1427. https://doi.org/10.1093/gji/ggz207

Revil, A., Schmutz, M., Abdulsamad, F., Balde, A., Beck, C., Ghorbani, A., & Hubbard, S. (2021). Field-scale estimation of soil properties from spectral induced polarization tomography. *Geoderma*, *403*, 115380. https://doi.org/10.1016/j.geoderma.2021.115380

Robinson, D. A. (2004a). Calculation of the dielectric properties of temperate and tropical soil minerals from ion polarizabilities using the clausius-mosotti equation. *Soil Science Society of America Journal*, *68*(5), 1780–1785. https://doi.org/10.2136/sssaj2004.1780

Robinson, D. A. (2004b). Measurement of the solid dielectric permittivity of clay minerals and granular samples using a time domain reflectometry immersion method. *Vadose Zone Journal*, *3*(2), 705–713. https://doi.org/10.2136/vzj2004.0705

Robinson, D. A., & Friedman, S. P. (2003). A method for measuring the solid particle permittivity or electrical conductivity of rocks, sediments, and granular materials. *Journal of Geophysical Research*, *108*(B2), 2076. https://doi.org/10.1029/2001JB000691

Robinson, D. A., Jones, S. B., Wraith, J. M., Or, D., & Friedman, S. P. (2003). A review of advances in dielectric and electrical conductivity measurement in soils using time domain reflectometry. *Vadose Zone Journal*, *2*(4), 444–475. https://doi.org/10.2136/vzj2003.4440

Rodrigues, C. D., Brito, L. M., & Nunes, L. J. R. (2023). Soil carbon sequestration in the context of climate change mitigation: A review. *Soil Systems*, *7*(3), 64. https://doi.org/10.3390/soilsystems7030064

Santamarina, J. C., Rinaldi, V. A., Fratta, D., Klein, K. A., Wang, Y.-H., Cho, G. C., & Cascante, G. (2012). 4. A survey of elastic and electromagnetic properties of near-surface soils. In *Near-surface geophysics* (pp. 71–88). https://doi.org/10.1190/1.9781560801719.ch4

Schmidt, F., Wagner, N., Landmark, S., & Bumberger, J. (2021). Impact of the cation exchange capacity on dielectric relaxation spectra of water saturated clays. In *13th international conference on electromagnetic wave interaction with water and moist substances (ISEMA)* (pp. 1–7). https://doi.org/10.1109/ISEMA49699.2021.9508335

Schmidt, F., Wagner, N., Mulder, I., Emmerich, K., Bore, T., & Bumberger, J. (2025). Broadband dielectric analysis of clays: Impact of cation exchange capacity, water content, and porosity [Dataset]. *Zenodo*. https://doi.org/10.5281/zenodo.15473270

Schön, J. H. (2015). *Physical properties of rocks: Fundamentals and principles of petrophysics*. (2nd edn). Elsevier.

Schwartz, N., & Furman, A. (2014). On the spectral induced polarization signature of soil organic matter. *Geophysical Journal International*, *200*(1), 589–595. https://doi.org/10.1093/gji/ggu410

Schwing, M., Wagner, N., Karlovsek, J., Chen, Z., Williams, D. J., & Scheuermann, A. (2016). Radio to microwave dielectric characterisation of constitutive electromagnetic soil properties using vector network analyses. *Journal of Geophysics and Engineering*, *13*(2), S28–S38. https://doi.org/10.1088/1742-2132/13/2/S28

Seigel, H. (1959). Mathematical formulation and type curves for induced polarization. *Geophysics*, *24*(3), 547–565. https://doi.org/10.1190/1.1438625

Sihvola, A. (Ed.) (2000). *Electromagnetic mixing formulas and applications*. INSPEC, Inc.

Soueid Ahmed, A., Revil, A., Abdulsamad, F., Steck, B., Vergniault, C., & Guihard, V. (2020). Induced polarization as a tool to non-intrusively characterize embankment hydraulic properties. *Engineering Geology*, *271*, 105604. https://doi.org/10.1016/j.enggeo.2020.105604

Steffen, W., Richardson, K., Rockström, J., Cornell, S. E., Fetzer, I., Bennett, E. M., et al. (2015). Planetary boundaries: Guiding human development on a changing planet. *Science*, *347*(6223), 1259855. https://doi.org/10.1126/science.1259855

Steudel, A., Batenburg, L. F., Fischer, H. R., Weidler, P. G., & Emmerich, K. (2009). Alteration of swelling clay minerals by acid activation. *Applied Clay Science*, *44*(1–2), 105–115. https://doi.org/10.1016/j.clay.2009.02.002

Stokes, M. R., Yang, Z. E., Ezebuiro, P., & Fischer, T. (2020). A new CEC-measurement proxy using high-frequency dielectric analysis of crushed rock. *Petrophysics*, *61*(2), 179–188. https://doi.org/10.30632/PJV61N2-2020a4

Storn, R., & Price, K. (1997). Differential evolution–A simple and efficient heuristic for global optimization over continuous spaces. *Journal of Global Optimization*, *11*(4), 341–359. https://doi.org/10.1023/A:1008202821328

Stroud, D., Milton, G. W., & De, B. R. (1986). Analyticael for the dielectric response of brine-saturated rocks. *Physical Review B*, *34*(8), 5145–5153. https://doi.org/10.1103/PhysRevB.34.5145

Taherian, M. R., Kenyon, W. E., & Safinya, K. A. (1990). Measurement of dielectric response of water-saturated rocks. *Geophysics*, *55*(12), 1530–1541. https://doi.org/10.1190/1.1442804

Tarantola, A. (2005). *Inverse problem theory and methods for model parameter estimation*. Society for Industrial and Applied Mathematics. https://doi.org/10.1137/1.9780898717921

Tombácz, E., & Szekeres, M. (2006). Surface charge heterogeneity of kaolinite in aqueous suspension in comparison with montmorillonite. *Applied Clay Science*, *34*(1), 105–124. https://doi.org/10.1016/j.clay.2006.05.009

Topp, G. C., Davis, J. L., & Annan, A. P. (1980). Electromagnetic determination of soil water content: Measurement in coaxial transmission lines. *Water Resources Research*, *16*(3), 574–582. https://doi.org/10.1029/WR016i003p00574

Tournassat, C., & Steefel, C. I. (2019). Reactive transport modeling of coupled processes in nanoporous media. *Reviews in Mineralogy and Geochemistry*, *85*(1), 75–109. https://doi.org/10.2138/rmg.2019.85.4

Triantafilis, J., Lesch, S. M., La Lau, K., & Buchanan, S. M. (2009). Field level digital soil mapping of cation exchange capacity using electromagnetic induction and a hierarchical spatial regression model. *Australian Journal of Soil Research*, *47*, 651–663. https://doi.org/10.1071/SR08240

United Nations General Assembly. (2015). Transforming our world: The 2030 agenda for sustainable development. Retrieved from https://sdgs.un.org/2030agenda

Vilhelmsen, T. B., Grayver, A. V., & Døssing, A. (2024). Drone-towed electromagnetic and magnetic systems for subsurface characterization and archaeological prospecting. *Near Surface Geophysics*, *22*(6), 617–635. https://doi.org/10.1002/nsg.12320

Vogel, H.-J., Weller, U., & Schlüter, S. (2024). *Chapter six - Linking structure and functions in agricultural soils*. In D. L. Sparks (Ed.), (Vol. 188, pp. 363–403). Academic Press. https://doi.org/10.1016/bs.agron.2024.06.005

Vrugt, J. A., Gupta, H. V., Bouten, W., & Sorooshian, S. (2003). A shuffled complex evolution metropolis algorithm for optimization and uncertainty assessment of hydrologic model parameters. *Water Resources Research*, *39*(8), 1201. https://doi.org/10.1029/2002WR001642

Wagner, N., Bore, T., Robinet, J., Coelho, D., Taillade, F., & Delepine-Lesoille, S. (2013). Dielectric relaxation behavior of callovo-oxfordian clay rock: A hydraulic-mechanical-electromagnetic coupling approach. *Journal of Geophysical Research: Solid Earth*, *118*(9), 4729–4744. https://doi.org/10.1002/jgrb.50343

Wagner, N., Emmerich, K., Bonitz, F., & Kupfer, K. (2011). Experimental investigations on the frequency-and temperature-dependent dielectric material properties of soil. *IEEE Transactions on Geoscience and Remote Sensing*, *49*(7), 2518–2530. https://doi.org/10.1109/tgrs.2011.2108303

Wagner, N., & Scheuermann, A. (2009). On the relationship between matric potential and dielectric properties of organic free soils: A sensitivity study. *Canadian Geotechnical Journal*, *46*(10), 1202–1215. https://doi.org/10.1139/T09-055

Wagner, N., & Scheuermann, A. (2017). Electromagnetic techniques in geoenvironmental engineering. *Environmental Geotechnics*, *4*(1), 3–8. https://doi.org/10.1680/envgeo.13.00104

Wagner, N., Schwing, M., & Scheuermann, A. (2014). Numerical 3-D FEM and experimental analysis of the open-ended coaxial line technique for microwave dielectric spectroscopy on soil. *IEEE Transactions on Geoscience and Remote Sensing*, *52*(2), 880–893. https://doi.org/10.1109/TGRS.2013.2245138

Wang, J., & Schmugge, T. J. (1980). An empirical model for the complex dielectric permittivity of soils as a function of water content. *IEEE Transactions on Geoscience and Remote Sensing*, *18*(4), 288–295. https://doi.org/10.1109/TGRS.1980.350304

Weigand, M., & Kemna, A. (2016). Debye decomposition of time-lapse spectral induced polarisation data. *Computers & Geosciences*, *86*, 34–45. https://doi.org/10.1016/j.cageo.2015.09.021

Weil, R., & Brady, N. (2017). The nature and properties of soils (15th ed.).

Wensink, W. (1993). Dielectric properties of wet soils in the frequency range 1–3000 MHz. *Geophysical Prospecting*, *41*(6), 671–696. https://doi.org/10.1111/j.1365-2478.1993.tb00878.x

Williams, G., & Watts, D. C. (1970). Non-symmetrical dielectric relaxation behaviour arising from a simple empirical decay function. *Transactions of the Faraday Society*, *66*, 80–85. https://doi.org/10.1039/TF9706600080

Yoon, T. J., Maerzke, K. A., Currier, R. P., & Findikoglu, A. T. (2023). PyOECP: A flexible open-source software library for estimating and modeling the complex permittivity based on the Open-Ended Coaxial Probe (OECP) technique. *Computer Physics Communications*, *282*, 108517. https://doi.org/10.1016/j.cpc.2022.108517

Zacharias, S., Loescher, H. W., Bogena, H., Kiese, R., Schrön, M., Attinger, S., et al. (2024). Fifteen years of integrated terrestrial environmental observatories (TERENO) in Germany: Functions, services, and lessons learned. *Earth's Future*, *12*(6), e2024EF004510. https://doi.org/10.1029/2024EF004510

Zhang, J., Clennell, M. B., Josh, M., & Pervukhina, M. (2020). Frequency and water saturation dependency of dielectric properties of clay mineral. *Applied Clay Science*, *198*, 105840. https://doi.org/10.1016/j.clay.2020.105840